Supplementary Information for

Pulsatory volcanism in the Main Ethiopian Rift and its environmental consequences

Zara Franceschini[1]*, Raffaello Cioni[1,2], Stéphane Scaillet[3], Gaëlle Prouteau[3], Giacomo Corti[2], Federico Sani[1,2], Alessandro Mondanaro[1], Diletta Frascerra[3], Abate A. Melaku[4,5], Bruno Scaillet[3], Clive Oppenheimer[6], Florian Duval[3]

[1]Dipartimento di Scienze della Terra, Università degli Studi di Firenze, Florence, Italy.
[2]Istituto di Geoscienze e Georisorse, Consiglio Nazionale delle Ricerche, Florence, Italy.
[3]Institut des Sciences de la Terre d'Orléans, UMR 7327 INSU-CNRS-BRGM – Université d'Orléans, Orléans, France.
[4]School of Earth Sciences, Addis Ababa University, Addis Ababa, Ethiopia.
[5]School of Earth and Environmental Sciences, University of St Andrews, St Andrews, United Kingdom.
[6]Department of Geography, University of Cambridge, Cambridge, United Kingdom.

*Corresponding author. Zara Franceschini (zara.franceschini@unifi.it)

This PDF file includes:

Supplementary Methods 1 and 2
Supplementary Discussions 1 to 3
Supplementary Figures 1 to 11
Supplementary Tables 1 to 3

Other Supplementary Materials for this manuscript include the following:

Supplementary Data 1 to 4

Supplementary References

Supplementary Method 1. Statistical analysis

A statistical analysis aimed at recognising the time distribution (homogeneous vs. clustered) of volcanism was adopted both for our new geochronological data on CMER and for a critically revised dataset on regionally distributed tephra in the last 4 Ma. The Inter-event Interval Histogram (IIH), the coefficient of variation (Cv) and the Allan Factor (AF) tests[1,2,3] were applied at the two datasets. The C_v is defined as:

$$C_v = {(\sigma_T)}/{\langle T \rangle}$$

Where ⟨T⟩ is the mean of the interevent time and (σ_T) its standard deviation. For a Poisson process (completely random) C_v= 1, while C_v> 1 characterizes more clustered statistical distributions, and C_v< 1 is typical for more "regular" time occurrence (C_v= 0 indicates a perfect periodicity of the process)[3].
For the CMER dataset, C_v has a value of 1.75, which suggests a clustered statistical distribution of the eruptions. Analogously, the value calculated for the time distribution of regional tephra is >1 (C_v= 1.23).

The IIH test (Supplementary Figure 2) confirms the inherent clustering of the events in the two datasets, since data are well fitted by a power law function (typical of clustered events) rather than by an exponential function (typical of Poissonian, more regularly spaced events).

Finally, clustering of the regional tephra was also tested through the application of the Allan Factor[2], for which the AF value is defined as

$$AF_T = \frac{< (N_{k+1(T)} - N_{k(T)})^2 >}{2 < N_{k(T)} >}$$

where the numerator is the average variance of successive counts for a specified counting time T and the denominator is twice the mean number of events in that counting time[1]. An AF increasing with the counting time T (Supplementary Figure 3) results in a calculated alfa value for the power law fit > 0, so again confirming the temporal clustering of the examined events.

Supplementary Method 2. Volume estimation

A precise determination of the volumes involved in each single large eruptions identified in the area is largely hampered by the lack of continuity of the outcrop exposures. These are mainly present along the rift margins, while the thick covering related to younger products on the rift floor represents an obstacle for the definition of the average thickness in this sector and of the real dispersal toward North and South of the study area.
By considering the cluster of intense volcanism as a whole, we can however provide an order of magnitude estimation of the total volumes of material emplaced during the silicic volcanic clusters of the Pliocene and Early Pleistocene respectively. For the volume of the youngest pulse of silicic explosive volcanism, we consider the estimated value defined by Hutchison et al.[4]. The acquired data were on the contrary not sufficient to provide an estimation of the minimum volume of the deposits involved in the other volcanic phases recognised in this study. The areas interested by the

products of the Pliocene and Early Pleistocene volcanic clusters are reported in Supplementary Figure 4. The dotted line marks the area beyond which the occurrence of the ignimbrites belonging to the cluster is uncertain, indicating that we do not exclude their possible further dispersion outside this area.

Volume estimation of the Pliocene silicic volcanic cluster

The minimum thicknesses of the deposits observed in the field are reported for each investigated site of both margins (Supplementary Figure 4). For the altered crystal-rich ignimbrite occurring within the geothermal wells of Aluto-Langano, we considered the thickness of ~400 m defined by previous study[5]. By considering the areal dispersion of the products and the thicknesses observed on the two margins and within the rift floor at Aluto-Langano wells, a minimum approximated volume for the deposits of the Pliocene Ignimbrites is estimated as the volume of the 3D Delaunay triangulation (obtained using a dedicated MatLab routine) of the points of thickness shown in Supplementary Figure 4a. We estimate that during the Pliocene, a minimum volume of at least 740 km^3 of deposit was emplaced in the CMER. Considering an average density of 1800 kg m^{-3} as representative of these densely welded to poorly welded ignimbrites[6], and a melt density of 2300 kg m^{-3} for the rhyolitic magma[7,8], we obtain a volume of Dense Rock Equivalent (DRE volume) of about 580 km^3, which however most likely largely underestimates the real volume involved. The visible thickness (considered in the abovementioned volume estimation) of 60 m for the MCT cropping out at C2, is indeed just a small portion of the whole deposit. Based on the inferred similarities between the facies sequence at site C2 and that of the complete outcrop at site G2 (about 20 km to the South; Supplementary Figure 4a) and their similar distances from the Aluto wells (where the maximum thickness of the deposit is recorded), we can assume that at site C2 the MCT possibly continues for several tens of metres below the surface exposed by the fault, presenting a thickness more or less equivalent to the one characterizing the outcrop at site G2 (~ 200 m). Moreover, the MCT is assumed to reach at least the Asela fault escarpment (about 30 km NNE of C2), where its observation is likely hampered by slope debris and vegetation covering of the basal 200 m of the fault escarpment. We consider therefore a theoretical point X (West of Kulumsa in Supplementary Figure 4a) at the northern tip of the Asela fault and assign to it a hypothetical thickness of 100 m. The distance separating this point from the Aluto wells is indeed little more than twice the distance between C2 and Aluto and we assume therefore that the thickness of the MCT at point X (if exposed on the surface) would be at least the half of the thickness shown at the Munesa-Langano escarpment. In this case we could estimate a maximum deposit volume (which most likely still represents a minimum "maximum volume") of the order of 1110 km^3 (~870 km^3 DRE volume).

This volume estimation does not take into account the amount of total extension occurred in the rift area since the emplacement of the first of the investigated Pliocene Ignimbrites. Giving the extensional geological setting, we should indeed consider that around 3.85 Ma the rift was not as wide as the ~ 100 km present-day transversal length of this sector of the rift, so implying a reduction of the area presently impacted by the ignimbrite dispersal. If we consider the extensional rate of ~ 5 mm yr^{-1} defined by Stamps et al.[9] for the MER and assume that this extension rate stayed constant through time (so applying the most conservative assumption in terms of uncertainty on volume estimation), the maximum linear extension which may have occurred since 3.85 Ma is ~ 20 km. This implies a maximum extension of about 25 %, which results in a volume overestimation of the same amount. This percentage is comparable to the uncertainty given by the deposit volume estimation of 740-1110 km^3 and can be considered enclosed within the suggested range value.

Volume estimation of the Early Pleistocene silicic volcanic cluster

Field observations and directional data collected from the Kencherra Ignimbrite[10] suggest a provenance from the central portion of the rift pointing to the Gademotta caldera, whose oldest products date back to ~1.26-1.29 Ma[11].

To define a minimum volume for the Early Pleistocene cluster, we decided to assign a minimum thickness of 20 m (similar to the average thickness observed for the Kencherra Ignimbrite along the eastern margin) at Gademotta, and a runout of the ignimbrites of at least 50 km (distances between the outcrops of the Kencherra Ignimbrite on the eastern plateau and Gademotta; white dotted line in Supplementary Figure 4b). The proposed areal dispersion of the products and the thicknesses observed at the outcrops, suggest that a minimum volume of about 50 km^3 of deposit (DRE volume of about 40 km^3, obtained by considering the same density values for the deposit and melt as used for the DRE volume calculation of the Pliocene Ignimbrites cluster) was emplaced during this volcanic phase, impacting the eastern margin and the rift floor. For the calculation of the minimum volume of this cluster (following the same procedure described for the Pliocene Ignimbrites), we consider in this case the dispersal area comprised between the entire outcropping ridge of Gademotta caldera (indicated with points X in Supplementary Figure 4b) and the investigated sites described along the eastern margin. Evidence of ~1.2 My old products occur also in the western margin of the rift, represented by two welded ignimbrites cropping out in the Worabe sector (at least 10 m in thickness) and by a poorly welded ignimbrite observed at Kella (> 20 m thick deposit). However, the reconstruction of the areal dispersion of these ignimbrites, and thus their volumetric contribution to the 1.29-1.16 Ma volcanic cluster, is hampered by the lack of continuous outcrops. These ignimbrites are reported in Supplementary Figure 4b just to evidence the coeval occurrence of large ignimbrite deposits on both margins of the rift and to state that the volumes of material emplaced during this cluster is most likely much larger than the suggested minimum value. To give a rough estimation of the possible maximum volume emplaced during this volcanic phase, the two deposits of the western margin were considered as witnesses of the extension of this volcanic activity to the whole central sector of the rift, thus resulting in an estimated deposit volume of the order of at least 120 km^3 (about 90 km^3 DRE volume).

By analogy to what done for the Pliocene Ignimbrites cluster, we applied a constant extensional rate for the rift of 5 mm yr^{-1} to evaluate the maximum linear extension that could have occurred in the last 1.3 Myr. It results in an overestimation of the volume by 7 % at most, an order of magnitude lower than the uncertainty enclosed in the estimated volume range of 50-120 km^3.

Supplementary Discussion 1. Distal tephra

Co-ignimbrite ash volume related to large ignimbritic eruptions is estimated to represent at least 30-40 % of the total erupted material[12-16]. Similarly, the considerable thickness and volumes of proximal deposits of the major ignimbrites recognized and dated in the CMER, imply large volumes of co-ignimbrite ashes that potentially impacted large zones well beyond the extent of the deposits we see today. With the aim of checking the occurrence of a time clustering of large explosive events similar to that observed in the present study for CMER activity, a critical review of the existing literature on distal tephra layers recognized and described at the scale of the whole MER and surrounding areas was undertaken. For this analysis, tephra beds occurring in distinct sites in the Turkana Basin[17-28], Omo Basin[20-24,26,28-30], Southern and Central MER[24,25,31-35], Awash Valley and SW Afar[19,27,36-39], as well as in the marine record in the Arabian Sea and Gulf of Aden[40-42] were considered. The locations of the investigated areas are reported in Supplementary Figure 5.

Geochronological and geochemical-based correlations among tephra layers located in distinct areas were considered to present a synoptic view summarizing the results of all these works (Supplementary Figure 6). As a first step, we considered ages determined through different dating techniques (K/Ar, $^{40}Ar/^{39}Ar$, fission track age, interpolated age model and orbitally tuned age); all these ages, with corresponding reference, are reported in Supplementary Data 1. However, to keep high the homogeneity and comparability of the analysed data, in selecting a single age for each event we preferred, where possible, those collected with $^{40}Ar/^{39}Ar$ dating technique over other methods. Moreover, when multiple $^{40}Ar/^{39}Ar$ ages were available, we favoured younger ages, more recent publications and/or publications where previous published ages were recalculated by the authors following updated refinement of the 40K decay constant[27] and of the fluence monitor standard[39]. In Supplementary Data 1, correlated tephra are grouped together, reporting in bold the preferred age (i.e., age considered representative of this eruptive event and used for data plotting in Supplementary Figure 5). Asserted correlations and ages are shown in Supplementary Figure 6.

These critically revised data clearly show a clustered distribution, that was here tested applying a statistical analysis for time-clustering of natural events[1,2]. The different statistical tests were evaluated to discriminate between Poissonian, homogeneous or clustered event distributions. All the three measures are concordant at indicating a clustered distribution of the events (see Supplementary Method 1 for detail). We interpret the differences in the duration of the periods of no activity observed in the time distribution of the regional tephra layers respect to those identified for the high intensity volcanism in the CMER (Fig. 3; Supplementary Figure 6) as the possible result of multiple sources in the different sectors of the MER for which the clusters of activity were slightly shifted in time.

In terms of possible correlations of the distal tephra layers with the main events recognised in the CMER stratigraphy, age and compositional data collected in the present study confirm the already proposed correlation of the MCT with the Tulu Bor Tuff of the Turkana Basin, to the Sidi Hakoma Tuff (SHT) occurring in the Hadar and in the Middle Awash and to tephra layers occurring within the drilled wells of the Gulf of Aden and Arabian Sea[27,43,44]. The age yielded by the MCT deposit is basically identical to the orbitally-tuned age of tephra layer ODP 722A-11-1[(ref.41)] and falls within the age range defined by the rest of the correlated deposits[27]. A chemical comparison between the main large ignimbrite deposits investigated within this study and the distal tephra reported in literature would result of utmost importance to further corroborate proposed geochronological correlations. Nevertheless, a preliminary attempt of comparing the existing geochemical data failed due to the complexity of comparing results obtained at different times and with different analytical methods, as well as for the lack of systematic trace elements data on glasses. Trace elements would indeed result much more indicative and, possibly, resolutive respect to EMPA major elements data given the specific glass composition generally buffered around the rhyolitic minimum.

The thickest tephra accumulation in the Pliocene marine record corroborates the occurrence of a major cluster of large-scale explosive volcanic eruptions during this period[42]. In contrast, tephra deposits of the following pulses occur mostly in trace quantities in DSDP Site 231, hinting at a lower-magnitude (lower volume) character of the more recent regional-scale eruptions[42]. The available distal record thus appears to support the hypothesis of a pulsatory behaviour of volcanism all along the MER likely with a direct contribution from some of the volcanic clusters now recognized in the CMER.

Supplementary Discussion 2. Human record

To define the First and the Last Appearance Datum (FAD and LAD, hereafter) of each hominin species, we implemented the human fossil dataset originally published in Timmermann et al.[51] by adding further Eastern African hominin occurrences. Specifically, we considered fossil occurrences belonging to the *Australopithecus*, *Paranthropus*, and *Kenyanthropus* species extending the temporal age interval in Timmermann et al.[51] back in time to ca. 4.5 Ma. Overall, we gathered 456 fossil occurrences restricted to East Africa which, according to the savannah hypothesis, represented the area where early evolution of our human ancestors occurred. We used two different approaches: one considering the specimens occurring in the whole East Africa (age intervals exemplified by the thin horizontal lines in Fig. 4b; this approach include all the hominin occurrences shown in Supplementary Figure 8) to provide a more comprehensive view of the hominin fossil record, the other considering only those occurrences (enclosed within the red ellipse in Supplementary Figure 8) restricted to the area (Ethiopia and surrounding areas) which could have been potentially impacted by the volcanic activity studied in this work (age intervals indicated by the coloured horizontal bars in Fig. 4b).

Australopithecus anamensis–afarensis is the oldest human lineage considered in the analyses. As FAD and LAD, we used 4.2 and 2.9 Ma respectively according to the estimated origination and extinction dates obtained by Du et al.[52] by accounting for dates uncertainty. The earliest available age for *A. anamensis* fossil record refers to the fossils yield of Kanapoi and Allia Bay Formation (Kenya)[53]. The youngest date is associated to the age determinations of the fossiliferous levels in Hadar Formation (Ethiopia)[54]. Intriguingly, the transition between *A. anamensis and A. afarensis* (3.8-3.6 Ma) falls within the first estimated major cluster of intense volcanic activity (Fig. 4) suggesting that volcanic and tectonic activities could have played a role for the early phase of hominin evolution.

The appearance of *A. deyiremeda* and *K. platyops* in the hominins fossil record coincides with the final step of the first volcanic cluster. Unfortunately, the record of *A. deyiremeda* is limited to the fossil remains recovered within a small, 3 km^2 wide area in Burtele, Woranso–Mille (Ethiopia)[55] whereas K. platyops is only known for the fossil specimens from the Lomekwi area (Kenya) dated 3.5-3.2 Ma[56].

A large number of hominins remains fall between the first and the second volcanic clusters suggesting that the decline of volcanic production and the establishment of a more stable tectonic conditions along the east African rift system could have prompted the human niche diversification and speciation.

Paranthropus includes three species but only two of them occurred in East Africa: *P. aethiopicus* and *P. boisei* whereby these two species possibly represent a single lineage. Fossils attributed to the former are radiometrically dated in between 2.7 and 2.3 Ma with the oldest specimens recovered from the Upper Ndolanya Beds, Silal Artum Locality, at Laetoli (Tanzania)[57] and the youngest within the Shungura Formation Member F (Ethiopia)[58]. *P. aethiopicus-P. boisei* transition is associated to morphological changes in the masticatory apparatus caused by an increased C4 food consumption[59]. The “robust” morphology characteristic of *P. boisei s*.s. is linked to the fossil specimens found in East Africa dated between 2.3 and 1.34 Ma[24] with the youngest specimen recovered from the Olduvai Gorge site, Bed II, in Tanzania[60].

Australopithecus garhi is considered a valid species after the description of a partial skull from the Hatayae Formation in Ethiopia’s Bouri Peninsula dated to 2.5 million years[61]. The phylogenetic relationships of *A. garhi* with the other hominins are uncertain although it was argued that Bouri hominin represented the sister taxon of a clade that includes *Homo*, *Paranthropus* and *A. africanus*[62].

The first members of Homo are *Homo habilis* and *H. rudolfensis*. The origin of genus Homo traced back to 2.8 Ma with the discovered of Ledi-Geraru mandible from Afar region, Ethiopia[63]. Villmoare and colleagues[63] provided the first morphological description of the mandible arguing that mandibular and dental traits aligned the specimen more closely with *H. habilis* than with any other hominid. Their findings and conclusions were questioned in later articles. Particularly, Neves et al.[64] performed a new morphometric comparative analysis of hominin mandibles suggesting that Ledi-Geraru is morphologically closer to *A. afarensis*, *H. erectus* and *A. sediba* than to earlier Homo members. Here we point out that the exact systematic position of the Ledi-Geraru mandible is out from the aims of this paper and prefer to stick with the original opinion of Villmoare and colleagues[63].

In contrast to FAD, the last appearance of *H. habilis* is temporally well constrained to the discoveries from MNK Skull sequence, Bed II, Olduvai Gorge dated at some 1.67 Ma[65].

Fossils ascribed to *Homo rudolfensis* are almost coeval to the *H. habilis* record. A semi-complete cranium associated to some postcranial bones were found in East Rudolf area, Koobi-Foora Formation, Kenya[66]. Overall, the age of these specimens ranged between 2 and 1.8 Ma[24,67]. However, the temporal bone from Chemeron Formation (Kenya) and the Uraha mandible from Malawi Rift tentatively attributed to *H. rudolfensis* extended the geographical distribution of this species toward the south along the Malawi Rift. Taking into account these remains, the species appearance is moved backward to 2.4of this species[68,69].

Homo ergaster record is well-attested in both East and South Africa. The FAD is associated to DNH 134 partial neurocranium from Drimolen Quarry in South Africa. The specimen was radiometrically dated at 2.04 Ma[70]. It is older than the *H. ergaster* specimens from Karari Ridge section, Koobi Foora Formation (Kenya) and the first appearance of Acheulean tools[71]. The LAD of *H. ergaster* is attested between 1 and 0.7 Ma but the scarcity of human fossil record within this time frame does not allow a more precise temporal estimation. Profico et al.[72] defined the origin of *H. heidelbergensis* at 875 Ka by analysing the large cranial fragments from Melka Kunture (Ethiopia). Consequently, the replacement of *H. ergaster* by *H. heidelbergensis* could be more likely restricted between 0.875 and 0.7 ka.

The last human species replacement reported in East Africa is the transition between *H. heidelbergensis* and *H. sapiens*. Human fossil record suggested that the appearance of our species in the Jebel Irhoud site (Morocco), radiometrically dated around 300 ka, marked the decline of *H. heidelbergensis*. Raia et al.[73] pointed out that this event temporally overlapped with the passage from Middle to the Late Stone Age technocomplex. Moreover, Timmermann et al.[50] built a climate envelope model to identify locations where potential succession or speciation of hominin groups may have taken place. The authors identified 300-200 ka as the most probable time window for *H.*

heidelbergensis-H. sapiens replacement according to habitat suitability values and archaeological artifacts. Furthermore, these time frame includes the recent $^{40}Ar/^{39}Ar$ dates used to constrain the age of Omo I, the oldest *H. sapiens* skull discovered in East Africa[30].

Similarly to *Australopithecus anamensis–afarensis*, the transition between *H. heidelbergensis* and *H. sapiens* seems associated to a time period with intense volcanic activity (Fig. 4).

Supplementary Discussion 3. Melt inclusions and volatiles

SEM used in Backscattered-Electron (BSE) Imaging on the selected crystals reveals different types of melt inclusions in the four samples, often enclosed within the same host-crystal. The first type consists of generally rounded-shaped, glassy melt inclusions which represent the best preserved and most suitable inclusions for analyses. Some elongated, irregular-shaped glassy melt inclusion with scattered or pronounced vesicularity can be observed as well, in some cases showing evidence of connection with the outer rim of the crystal and hence suggesting possible degassing caused by depressurization. Other rounded-shape, partially recrystallised inclusions occur as well, showing either spherulitic crystallisation decreasing in concentration from the edge of the otherwise glassy inclusion inward, or a recrystallised thin rim accompanied by sparse microcrystals scattered over the entire surface of the inclusion. Completely recrystallised and/or altered melt inclusions were excluded from the analyses. Melt inclusions size varies in the four samples but it generally ranges between 20 and 300 μm, with those belonging to samples ETZ136 showing the smaller range of size variation, between 20 and 100 μm. Matrix glass is occasionally preserved around some of the crystals.

Melt inclusion and matrix glass compositions are reported in Supplementary Data 2. The analysed melt inclusions sharply reflect the bimodal suite of the products, showing basaltic melt (SiO_2 ~47-48 wt.%) and rhyolitic melts ($72 < SiO_2 < 77$ wt.%) with no inclusion characterized by intermediate compositions (i.e., between 50 and 70 wt% SiO_2). The mafic inclusions occurring in plagioclase crystals of the Golja Ignimbrite (ETZ136) fall in the basalt field straddling the alkaline-subalkaline boundary line[74]. The evolved samples are peralkaline rhyolite, classified as either comendites or pantellerites: the melt inclusions belonging to the MCT are more comenditic in composition, those of the Kencherra Ignimbrite (sample ETZ30) are still comenditic but approach the comendite-pantellerite boundary line, while the rhyolitic melt inclusions of the Golja Ignimbrite (sample ETZ136) are clearly pantelleritic in composition. This trend matches the existing literature data which belongs to volcanic complexes that are all younger than the samples considered for this study[75].

The volatile compositions of each analysed melt inclusion and matrix glass are reported in Supplementary Data 2; averaged volatile concentrations, with the respective standard deviation, are reported for groups of melt inclusions (with "n" indicating the number of inclusions considered) in Supplementary Table 3. Melt inclusions belonging to the same sample are subdivided based on their host mineral (quartz, sanidine and plagioclase crystals) and melt inclusions enclosed in quartz crystals were further subdivided based on their characteristics (i.e., glassy, glassy vesicular, partially recrystallised…). The analyses of the groundmass glass are reported separately in Supplementary Table 3.

In line with literature data[75], estimated H_2O contents of all the analysed melt inclusions range between 0.8 and 8.5 wt.%, but differences are observed between the different samples and among different types of inclusions. Specifically, in sample ETZ31 (MCT), glassy vesicular inclusions have a water content which ranges between 0.8 and 4.2 wt.% (mean H_2O ~2.4 wt.%; Supplementary Table 3), with the inclusions showing the highest concentration of vesicles (and more likely connected with the surrounding melt) corresponding to those yielding the lowest values. Estimated H_2O content for the partially recrystallised inclusions of the same sample is instead significantly higher, varying between 4.0 and 5.7 wt. % (mean H_2O ~4.5 wt.%; Supplementary Table 3). The coexistence of these two different melt inclusions within the same crystals could possibly be explained by a loss of volatiles during decompression. Estimated H_2O content for the vesicle-free melt inclusions of sample ETZ90 (MCT) show a mean value around 2.9 wt.% (1.2 < H_2O < 4.4 wt.%), generally lower for glassy vesicular melt inclusions of the same sample which show a mean value around 2.3 wt.% (1.7 < H_2O < 2.8 wt.%; Supplementary Table3), similar to the glassy vesicular of sample ETZ31. Glassy melt inclusions in sample ETZ136 (Golja Ignimbrite) show different values of estimated water concentrations depending on the host crystal. Melt inclusions trapped in quartz and sanidine show higher concentrations (with mean values of 4.9 and 4.6 wt.% respectively; Supplementary Table 3), while for those embedded in plagioclases, the mean estimated H_2O content is around 2.96 wt.% (2.8 < H_2O < 3.3 wt.%). Finally, the partially recrystallised (spherulitic crystallisation) melt inclusions characterizing sample ETZ30 (Kencherra Ignimbrite), have (compared to the other melt inclusions) the narrowest range of water content between 3.8 and 5.0 wt.% (mean H_2O ~4.5 wt.%; Supplementary Table 3), very similar to the partially recrystallised melt inclusions of sample ETZ31. Cl mainly increases with Zr concentration showing more scattered values for melt inclusions having a Zr content around 1000 ppm (Supplementary Data 2). The basaltic melt inclusions trapped in plagioclase crystals of sample ETZ136 present the lowest Cl content (Cl concentrations proximal to 0). With the exception of two quartz-hosted melt inclusions of sample ETZ136 presenting high Cl and H_2O contents, the rest of the melt inclusions analysed from both quartz and sanidine crystals belonging to samples ETZ136, ETZ31 and ETZ90, are characterized by a relatively constant Cl content, oscillating around an average value of 0.13 wt.% (0.08 < Cl < 0.18 wt.%). On the contrary, melt inclusions belonging to sample ETZ30 have on average the highest Cl concentrations (between 0.2 and 0.27 wt.%; Supplementary Data 2 and Supplementary Table 3). F content is not reported for all the melt inclusions due to analytical problems encountered during measurements. SO_3 concentration is on average lower than 0.1 wt.% (i.e., less than 400 ppm S, most being around 100±50 ppm S) for almost all the melt inclusions but reaches values around 0.5 wt.% (nearly 2000 ppm S) in the basaltic melt inclusions trapped within plagioclases (of sample ETZ136; Supplementary Data 2).

Considering the whole set of melt inclusions, the following systematic appears: the population shows coherent trends between FeO (taken as a differentiation index) and H_2O, S and Cl contents. Starting at around 3 wt%, H_2O shows a continuous increase as FeO decreases, until reaching a maximum value of about 4-5 wt% H_2O at 4 wt% FeO, which could signal the attainment of H_2O saturation in the reservoir (Supplementary Figure 9). The decrease in H_2O seen at lower FeO contents might reflect decompression related crystallisation and exsolution.

Cl shows two possible trends: a trend first increasing from basalt to low silica rhyolite, reaching a maximum value of 3300 ppm Cl, perhaps mirroring brine saturation, thereafter decreasing down to values clustering around 1500 ppm Cl (Supplementary Figure 10). This late decrease may reflect Cl scavenging by a coexisting aqueous fluid phase. Alternatively, Cl may have increased steadily up to about 2000 ppm, after 90% crystallisation of basalt.

In contrast to these volatiles, sulphur shows a continuous decrease with FeO, from about 2000 ppm down to about 100 ppm, which is suggestive of its scavenging from the melt by sulphide saturation, possibly exacerbated at a later stage by concomitant fluid saturation (Supplementary Figure 11). Hence, the amount of S carried by the parental basalt was not entirely transferred to the felsic derivative.

Altogether, these observations suggest that the pre-eruptive temperature of comendite was at 700-800°C, to allow quartz and feldspar saturation at melt H_2O contents of 3-5 wt%[76], while reservoir pressure was at ca 1 kb which corresponds to the water saturation pressure for this class of silicate melts[77,78]. These conditions are typical for peralkaline rhyolites elsewhere[76,79-81].

The possible climatic effect of large-scale volcanic activity like that documented for some of the major clusters of activity in the CMER is not simple to evaluate. Data on the type and amount of volatile species released to the atmosphere during these periods can be derived estimating the net syn-eruptive volatile release to the atmosphere based on the comparison between pre-eruptive volatile content of the magma (inferred from melt inclusion trapped within growing crystals during magma crystallisation) and the residual volatile content of degassed melts (groundmass glass), as summarised above. However, depending on the crystals in which they are hosted, melt inclusions may witness different phases of the pre-eruptive magmatic evolution as well. Our data reveal no significant differences between the pre- and syn-eruptive melts (Supplementary Table 3) (i.e., between melt inclusion and matrix glass) and rather low concentrations of halogens (for the peralkaline, evolved magma compositions of the erupted products) (10-3 – 10-1 wt.% F; 10-2 – 10-1 wt.% Cl) and sulphur (10-3 – 10-1 wt.%) in the pre-eruptive melts. Taken at face value, this indicates a low relative amount of these species at eruption due to syn-eruptive degassing. In line with a study by Thines et al.[82] on the Afro-Arabian large igneous province, this evidence seems to suggest that these large ignimbrites, despite the drastic disruption of the surrounding environment which (due to their emplacement) they most likely caused, may have had a low impact in terms of sulphur and halogens release in the atmosphere and thus of major global environmental change, if not saturated in a fluid phase. However, evidence for the occurrence of a pre-eruptive free fluid phase in large magma reservoirs has been demonstrated in many cases[75,83-85] and should not be discarded. Our data indicate that the likely parental basaltic magma (found as inclusion in Pl) contained already 2-3 wt% H_2O. The ten-fold increase in Zr content between basalt and comendite inclusions indicates that comendite production requires at least 90% crystallisation of basalt. In view of the largely incompatible behaviour of water, this is more than sufficient for reaching water saturation in the reservoir, as discussed above based on the FeO-H_2O diagram. This fluid phase would have been indeed released in the atmosphere during the eruption but would go undetected in the products by conventional petrological methods. Part of this volatile budget was lost during magma storage, as suggested by the decrease in S and Cl contents, either due to pervasive degassing across magma chamber walls, or to mineral crystallisation (e.g., sulphide sequestration of S). We do not have constraints on the amount of pre-eruptive fluid but available evidence for silicic magmas suggests values in the range 1-5 wt%, including for comendite rhyolites[80,84]. The case of the Paektu eruption in 934 CE[(ref.79)] provides an interesting counterpart, because ejected rock shares many petrological attributes with Ethiopian comendites, in particular in terms of its pre-eruptive S content (around 91±51 ppm, excluding the low silica content rhyolite, compared to 110±3 ppm for Paektu) and storage conditions. The Paektu eruption ejected ca 23 km^3 of comendite rhyolite and is considered to have potentially released 45 Tg S[(ref.79)]. On this basis, a simple scaling up exercise for the Pliocene cluster (corresponding to a total DRE volume of 580-870 km^3 erupted in at least five major eruptions) shows that each eruption could have released about 200 Tg S, which is a figure 3-4 times higher than the S yield inferred for the famous Laki eruption[86], which was injected in about 8 months, however. As regards halogens, their lower amount in Ethiopian rhyolites compared to Paektu, suggests equally lower quantities of Cl and F emissions (inferred to be 20 and 58 Tg, respectively, for Paektu). We note that the amounts estimated by Iacovino et al.[79] assume fluid conservation (from trachyte to rhyolite), and hence have to be considered as maxima.

Regardless, the large, erupted volumes during each volcanic cluster could have been accompanied by the release of large amount of magmatic gases having a strong impact on climate, even with small volatiles contents in melt inclusions, underscoring the fact that the majority of volatiles in felsic magmas is hosted in the coexisting fluid phase at depth. Given the likely short duration of each single eruption we speculate, in agreement with other observations[87-92], that any such effect could have been of brief duration and had possibly important impact mainly at the local scale, superimposing on strongly compromised environmental conditions arising from the physical effects of the eruptions.

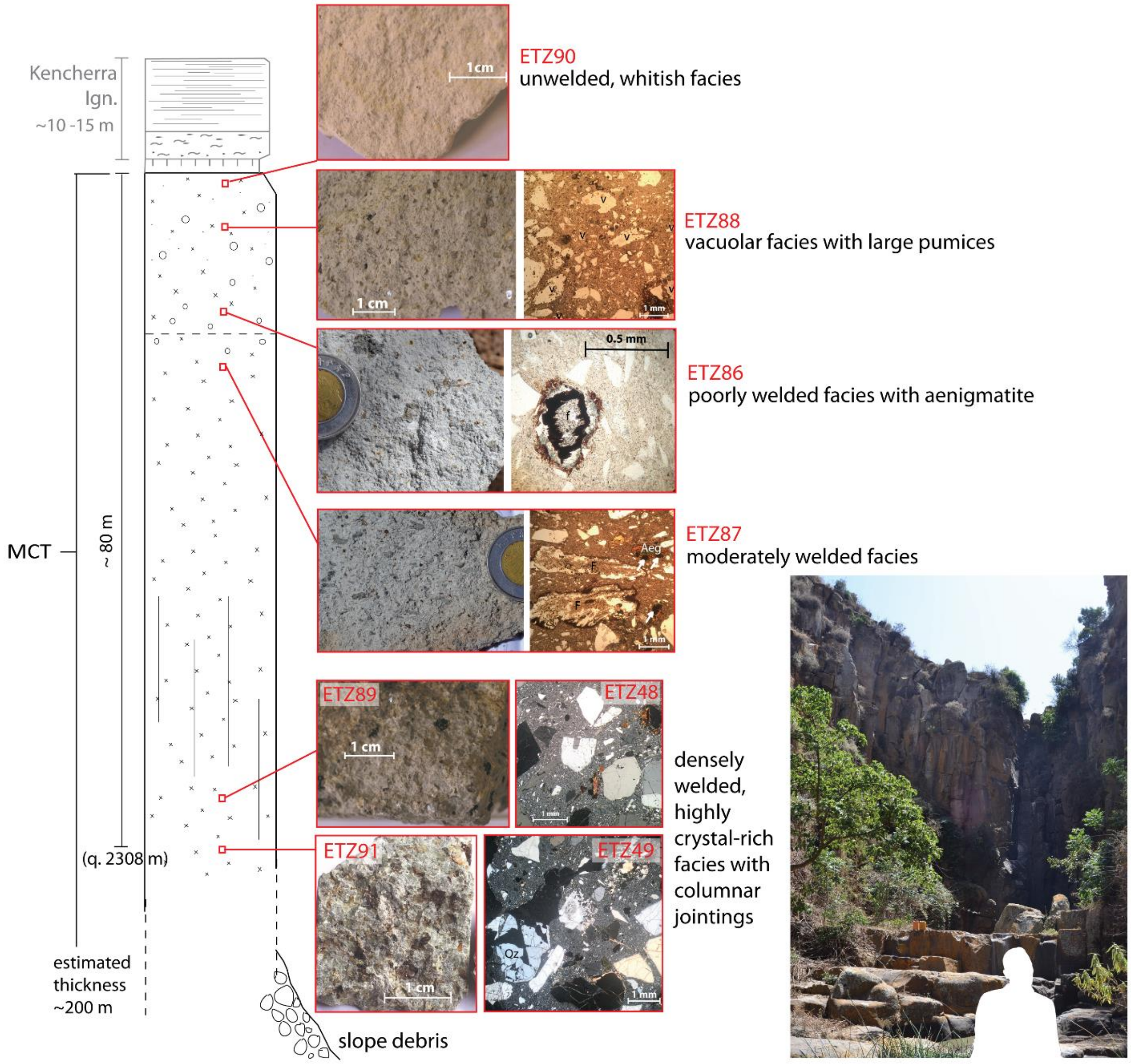

Supplementary Figure 1a. Type-section of the MCT s.s. at sampling site G3. The photo of the outcrop (bottom, right) was taken at sampling site G2. The stratigraphic column reports the samples collected at different elevation within the ignimbrite deposit. The different facies recognized facilitate the correlations with other outcrops of the same ignimbrite elsewhere. Examples of thin sections observed under the petrographic microscope are reported next to the corresponding samples/facies. V= micro- and mm-sized vesicles of different shapes; f= altered femic crystal with reaction rim and alteration halo; F= mm-sized recrystallized fiamme with jagged edges and reddish alteration halo; Aeg= aegirine crystal with altered rim; white arrows= sub-millimetric oxides; Qz= fractured quartz phenocryst.

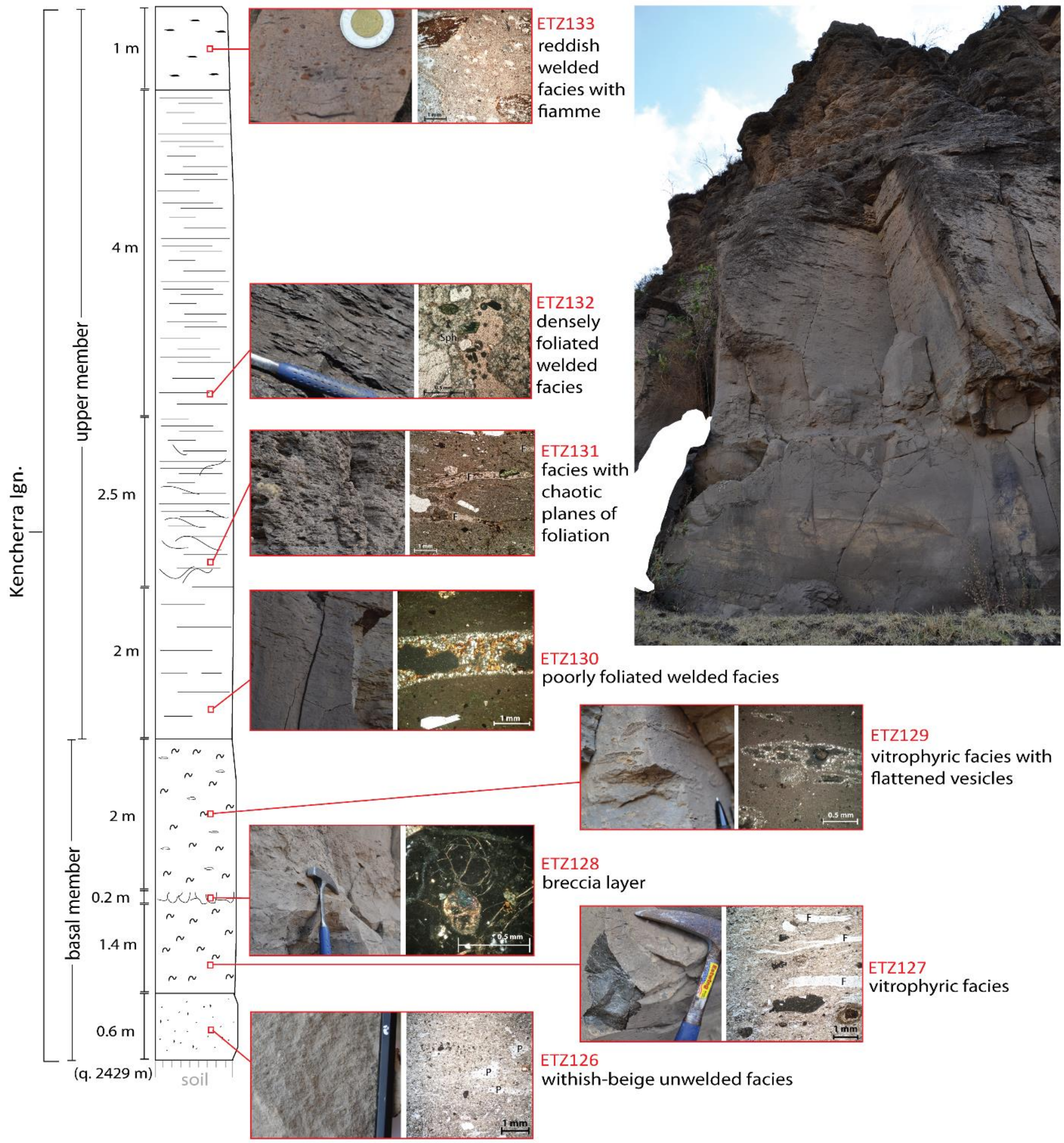

Supplementary Figure 1b. Type-section of the Kencherra Ignimbrite at sampling site E5. The photo of the outcrop (top, right) was taken from the same sampling site. The stratigraphic column reports the samples collected at different elevation within the ignimbrite deposit, which can be subdivided into two main members. The different, diagnostic facies recognized facilitate the correlations with other outcrops of the same ignimbrite elsewhere. Examples of thin sections observed under the petrographic microscope are reported next to the corresponding samples. P= pumices, both undeformed and partially flattened; F= fiamme; Sph= spherulitic recrystallization; S= scoria.

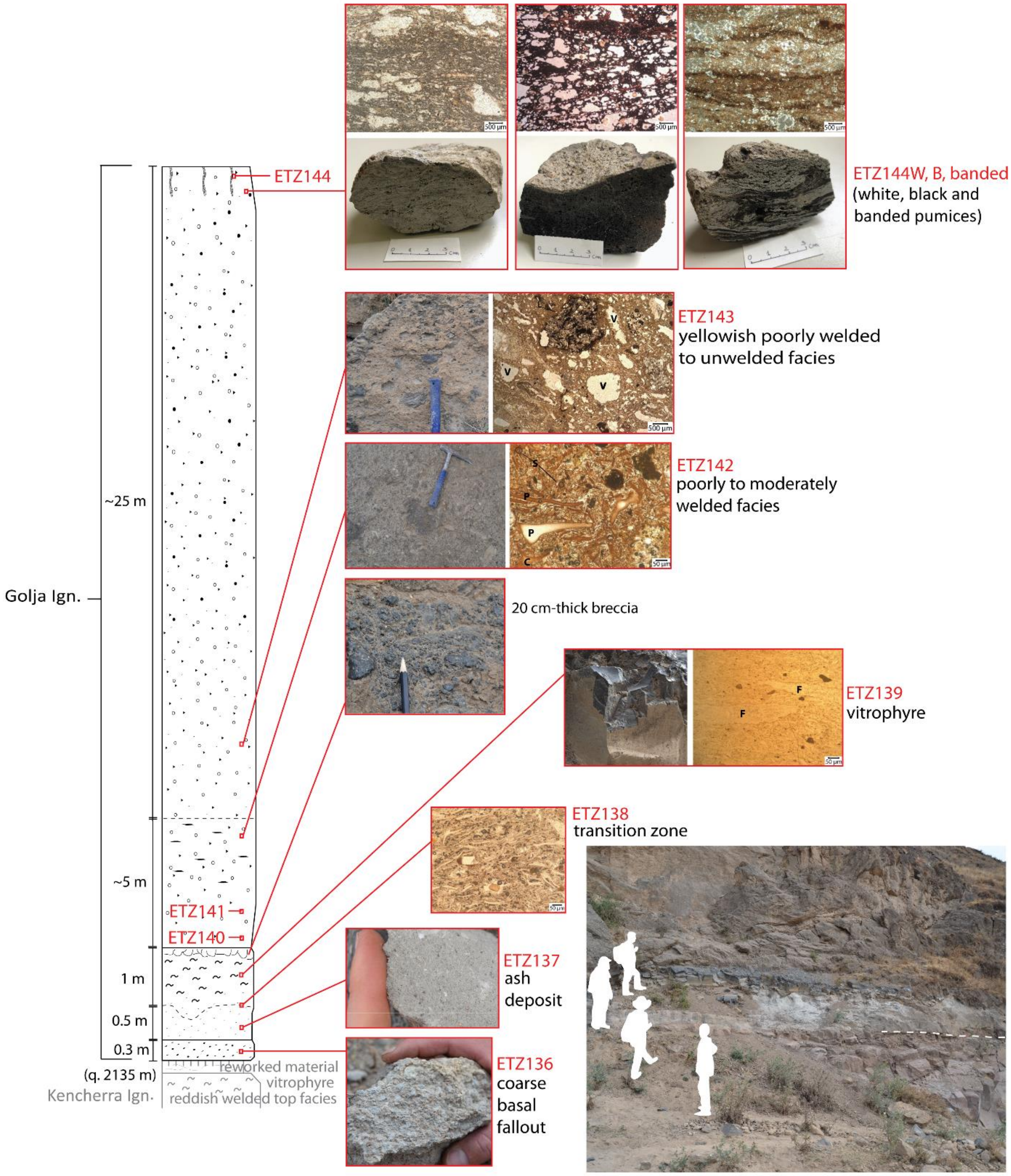

Supplementary Figure 1c. Type-section of the Golja Ignimbrite at sampling site C6. The photo of the outcrop (bottom, right) was taken from the same sampling site. The stratigraphic column reports the samples collected at different elevation within the ignimbrite deposit. The different facies recognized facilitate the correlations with other outcrops of the same ignimbrite elsewhere. Examples of thin sections observed under the petrographic microscope are reported next to the corresponding samples. F= fiamme with irregular rims; S= glassy spherules, C= Y-shape cuspate shards; P= platy shards; V= mm-sized irregular shaped vesicles.

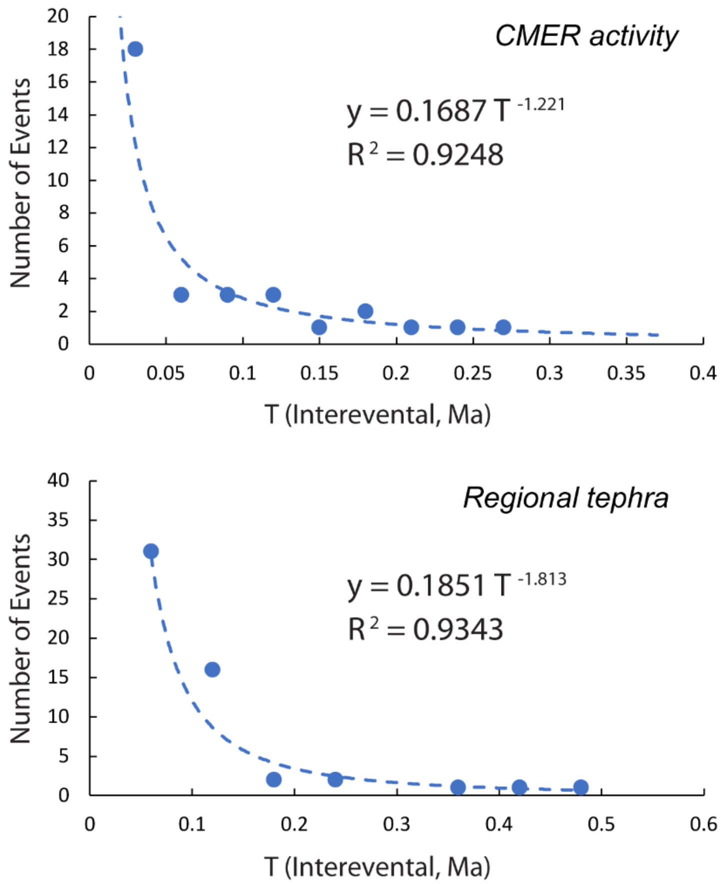

Supplementary Figure 2. Interevent-interval histogram. The fit is calculated for the most complete part of the diagram, for which all the adjacent intervals are populated; for the CMER data only 3 out of a total of 36 interevent ages are not considered for the fit.

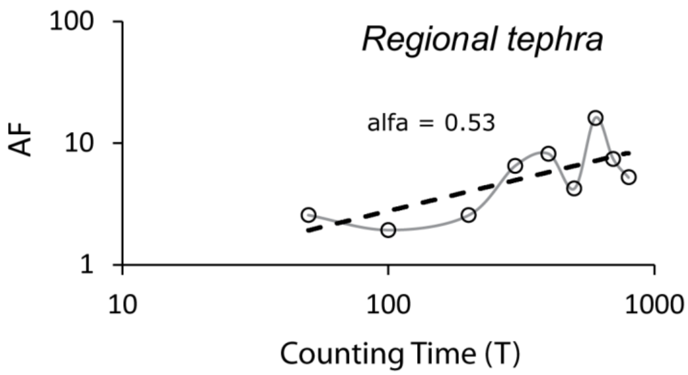

Supplementary Figure 3. Allan Factor as calculated for the regional tephra.

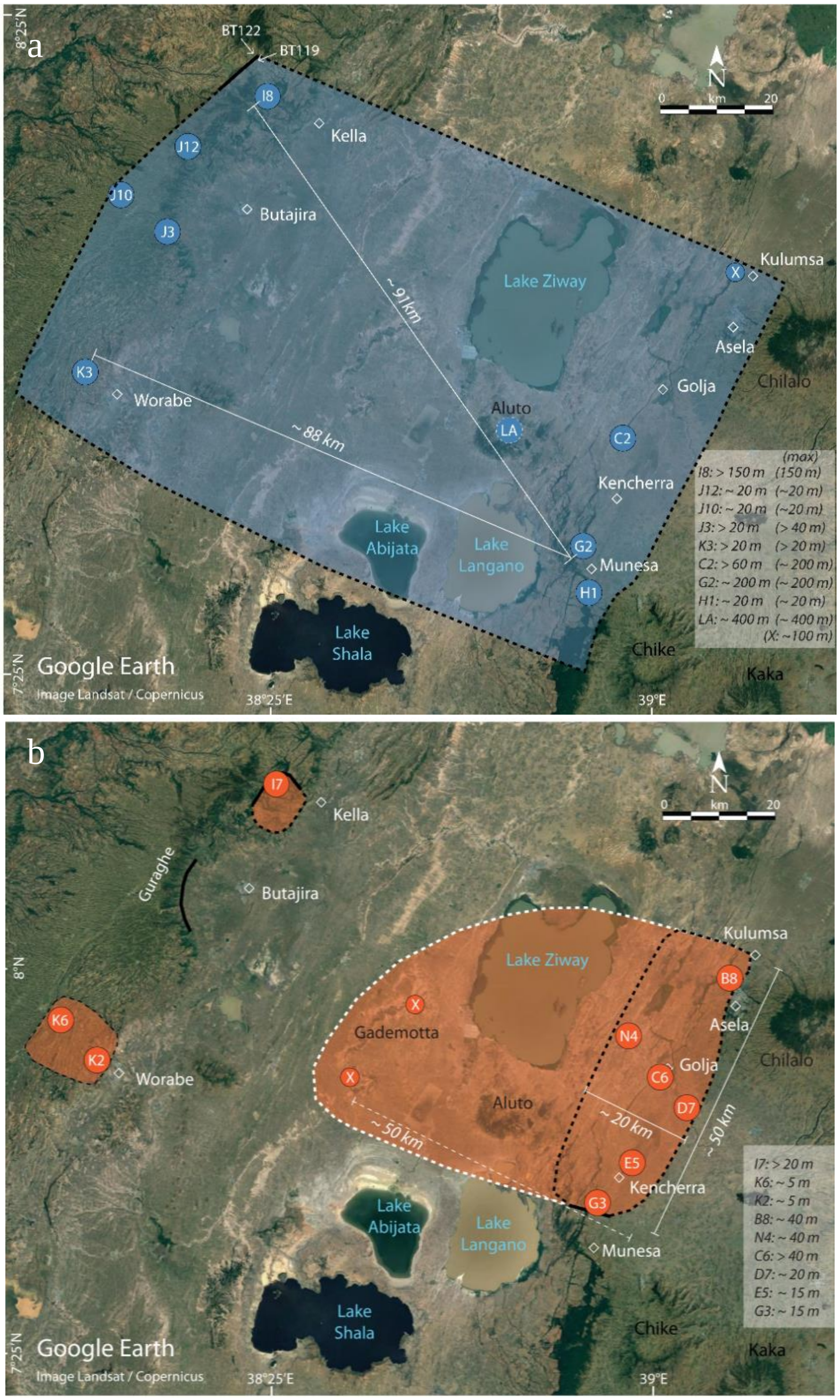

Supplementary Figure 4. Areas covered by the Pliocene silicic volcanic flare-up (a) and by the volcanic flare-up at 1.3-1.2 Ma (b). Minimum thicknesses of the deposits are reported from selected investigated sites (max thickness in brackets). The dotted line marks the area beyond which the ignimbrites occurrence is uncertain (their dispersion outside this area cannot be however excluded). The portions where the dotted black line becomes continue, indicate that there is evidence that the ignimbrites do not occur outside the area. Maps Data: Google, Image Landsat/Copernicus.

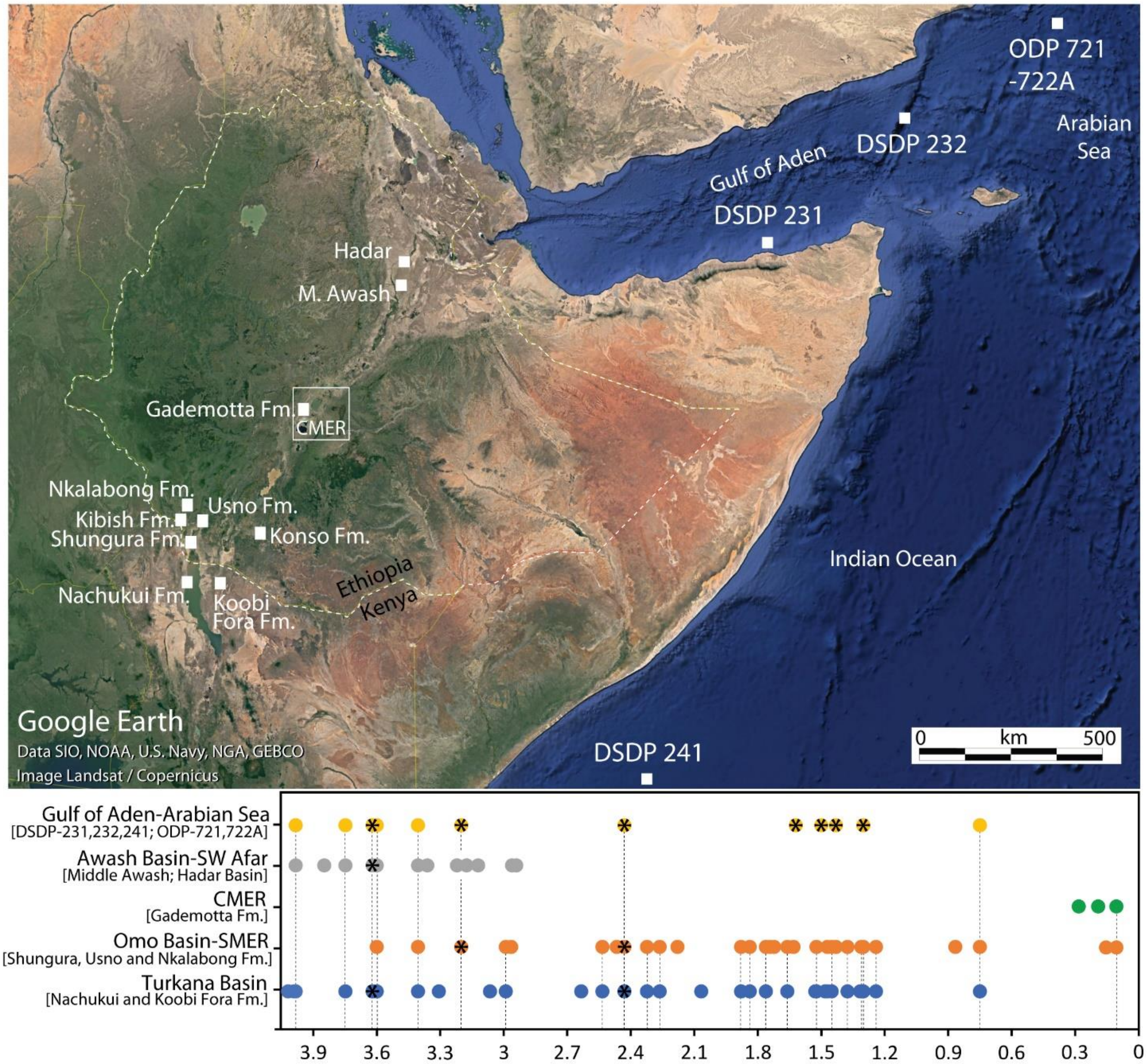

Supplementary Figure 5. Dated tephra layers locations between the Turkana Basin and the drilling wells in the Gulf of Aden and Arabian sea; the location of the considered sites of investigation is reported on the map; Ethiopia is indicated by a white dashed line. The dots represent $^{40}Ar/^{39}Ar$ ages; when marked by an asterisk, they indicate interpolated/estimated ages or orbitally-tuned ages. Established correlations between two or more deposits are marked with dotted lines connecting the different investigated sites (Supplementary Figure6; Supplementary Data 1). Maps Data: Google Earth, Data SIO, NOAA, U.S. Navy, NGA, GEBCO, Image Landsat/Copernicus.

	Turkana Basin		Omo Basin			SMER	CMER	Awash Basin - SW Afar		Gulf of Aden		Arabian Sea	Indian Ocean	CMER - PROXIMAL DEPOSITS/SOURCING VOLCANO
	Nachukui Fm.	Koobi Fora Fm.	Shungura Fm.	Usno Fm.	Nkalabong- Kibish Fm.	Konso-Gardula Fm.	Gademotta Fm.	Middle Awash	Hadar Basin	DSDP 231	DSDP 232	OSP 721 - 722A	DSDP 241	
0.105 ± 0.005 Ma (10)					***Alyio Tuff*** ★		Unit 15 ★							BBTM eruption ★ 0.108 ± 0.009 Ma (15)
0.154 ± 0.007 Ma (12)					18-09C	***Silver Tuff (SVT)*** ★								Shala eruption ★ 0.145- 0.155 Ma (16)
					18-08	TA-56								Corbetti eruption ★ 0.177 ± 0.008 Ma (14;16)
0.191 ± 0.004 Ma (8)							***Unit D*** ★							
					KHS Tuff									Shala eruption ★ 0.233 ± 0.022 Ma (16)
0.283 ± 0.003 Ma (8)							***Unit 10*** ★							
	Kale Tuff	Kale Tuff				956-11								
0.750 ± 0.02 Ma (11)		***Silbo Tuff*** ★				Upper White Tuff (UWT)				231-5CC			241-2-1-38	
		Naguli Tuff												
0.865 ± 0.059 Ma (11)						Baraisa Tuff-1 (BAT1) ★								GOLJA IGN. ★ 1.159 ± 0.006 Ma (17)
1.24 ± 0.02 Ma (11)	***U. Nariokotome Tuff*** ★					Piso Tuff-2 (PST-2)								
1.31 ± 0.03 Ma (11)	***M. Nariokotome Tuff*** ★					Piso Tuff-1 (PST-1)								KENCHERRA IGN. ★ 1.263 ± 0.004 Ma (17)
1.30 ± 0.03 Ma (11)	***L. Nariokotome Tuff*** ★					Boleshe Tuff (BOT)								
1.315 ± 0.002 Ma (13)		***Gele Tuff*** ★												
1.375 ± 0.002 Ma (13)	Chari Tuff	Chari Tuff ★	***Tuff L*** ★			Bright White Tuff (BWT) ★								
1.43 ± 0.05 Ma (11)						***Karat Tuff (KRT)*** ★								
~ 1.43 Ma (7)										***231-9-4*** ○				
1.47 ± 0.07 Ma (5)						***Lehyate Tuff (LHT)*** ★								
	Lokapetamoi Tuff					Ivory Tuff (IVT)								
1.45 ± 0.02 Ma (11)	Etirr Tuff					***Trail Bottom Tuff (TBT)*** ★								
1.47 ± 0.008 Ma (6)	***Ebei Tuff*** ★													
1.48 ± 0.006 Ma (6)		***Karari Blue Tuff*** ★												
1.481 ± 0.005 Ma (6)		***Koobi Fora Tuff*** ★												
1.478 ± 0.005 Ma (6)		***L. Koobi Fora Tuff*** ★												
~ 1.5 Ma (7)										***231-9-6*** ○				
1.522 ± 0.006 Ma (10)		Morte Tuff ★	***Tuff K*** ★			Iyanda Tuff (IDT) ★								
1.528 ± 0.005 Ma (6)		***Lower Ileret Tuff*** ★												CHEBI ASH FLOW ★ 1.545 ± 0.004 Ma (17)
~ 1.62 Ma (7)										***231-10-4*** ○				
1.63 ± 0.02 Ma (11)						***KGA19-Handaxe Tuff (19HAT)*** ★								
1.66 ± 0.06 Ma (11)	Morutot Tuff ★	Lower Okote Tuff	Tuff J4-1			***KGA19-Bench Tuff (NBT)*** ★								
1.722 ± 0.006 Ma (6)					***Chibele Tuff*** ★									
1.74 ± 0.06 Ma (10)						***Kayle Tuff-2 (KYT-2)*** ★								
1.761 ± 0.007 Ma (10)	Orange Tuff	***Orange Tuff*** ★	Tuff J			Kayle Tuff-1 (KYT-1) ★								
1.837 ± 0.001 Ma (13)	Malbe Tuff	Malbe Tuff ★	***Tuff H-4*** ★											
1.879 ± 0.001 Ma (13)	KBS Tuff	KBS Tuff ★	***Tuff H-2*** ★			Turoha Tuff ★								
2.067 ± 0.007 Ma (6)	***Kangaki Tuff*** ★													
2.179 ± 0.008 Ma (6)			***Tuff G-3*** ★											
2.262 ± 0.012 Ma (10)	Unnamed Tuff		***Tuff G*** ★											
2.323 ± 0.008 Ma (6)	Kalochoro Tuff ★		***Tuff F*** ★											
~ 2.43 Ma (1)	***Kokiselei Tuff*** ○		Tuff E							231-14-5-105	232-11-2-75			
2.466 ± 0.01 Ma (6)			***Tuff D-3-2*** ★											
2.533 ± 0.009 Ma (6)	***Lokalalei Tuff*** ★	***Lokalalei Tuff*** ★	Tuff D											
2.634 ± 0.013 Ma (13)		***Burgi Tuff*** ★												
2.94 Ma (9)									***BKT-2 U.*** ★					
2.96 Ma (9)									***BKT-2 L.*** ★					
2.99 ± 0.093 Ma (10)		Hasuma Tuff	***Tuff C*** ★											
2.965 ± 0.011 Ma (6)			***Tuff B-10-1*** ★											
3.064 ± 0.012 Ma (6)		***Ninikaa Tuff*** ★												
3.12 Ma (9)									***BKT-1 Complex*** ★					
3.175 ± 0.012 Ma (3)									***Kada Hadar Tuff (KHT)*** ★					
~ 3.2 Ma (1)				Karo Tuff						***231-18-3-147*** ○				
3.22 ± 0.01 Ma (3)									***Triple Tuff-4 (TT-4)*** ★					
3.306 ± 0.013 Ma (6)		***Toroto Tuff*** ★												
3.36 Ma (9)									***Kada Me'e Tuff*** ★					
3.405 ± 0.011 Ma (10)	Tulu Bor Tuff (α- β)	Tulu Bor Tuff (α- β) ★	***Tuff B-δ*** ★	Tuff U-10/11	Tuff B			MA90-28 (SHT) ★	Sidi Hakoma Tuff (SHT-41) ★	231-19-2-30		722A-11-1 ▲		MCT s.s. ★ 3.412 ± 0.004 Ma (17)
3.6 ± 0.024 Ma (6)	Lokochot Tuff	Lokochot Tuff	Tuff A	Tuff U-7	***Tuff A*** ★			MA02-5 ★	Kilaytoli Tuff (KT) ★	231-20-1 ○	232-16-4-10	722A-11-4 ▲		KELLA-BUTAJIRA IGN. ★ 3.537 ± 0.004 Ma (17)
										231-20-2-27	232A-1-4-44			
3.620 ± 0.010 Ma (4)	Logomol Tuff	Logomol Tuff						ERV 032			232A-1-5-27	***722A-11-5*** ▲		WORABE ASH FLOW ★ 3.605 ± 0.006 Ma (17)
3.748 ± 0.023 Ma (2)		Wargolo Tuff ○						***VT-3*** ★	Ikini Tuff	231-21-2-18 ○	232-18-1-80	721C-13-3 ▲		"H1.A" IGN. ★ 3.691 ± 0.007 Ma (17)
3.847 ± 0.083 Ma (2)								***Cindery Tuff (CT)*** ★						GURAGHE IGN. ★ 3.846 ± 0.007 Ma (17)
3.982 ± 0.012 Ma (6)	Moiti Tuff	***Moiti Tuff*** ★						VT-1 ★		231-22-1-82		722A-12-4 ▲	241-7CC	
3.991 ± 0.017 Ma (6)	***Topernawi Tuff*** ★													
4.018 ± 0.011 Ma (10)		***Naibar Tuff*** ★												

Supplementary Figure 6. Distal tephra correlation. Synoptic view of the existing literature on distal tephra layers recognized and described at the scale of the whole MER and surrounding areas. This figure was aimed at visually representing established correlations of tephra among the distinct areas. Established correlations among recognized tephra layers are evidenced by dotted red lines. Among the tephra which are correlated together, it is reported in italic and bold the tephra layer whose age was considered for data plotting in Supplementary Figure 5. The ages and corresponding references are reported in red on the left. 1) Brown et al.[20]; 2) White et al.[44]; 3) Walter[37]; 4) deMenocal and Brown[41]; 5) Katoh et al.[31]; 6) McDougall and Brown[21,22]; 7) Feakins et al.[42]; 8) Morgan and Renne[34]; 9) Roman et al.[38]; 10) McDougall et al.[24,29]; 11) Beyene et al.[25]; 12) Clark et al.[32]; 13) Phillips et al.[28]; 14) Hutchison et al.[4]; 15) Tadesse et al.[45]; 16) Vidal et al.[30,35]**.** Dated tephra layers are marked with a star ($^{40}Ar/^{39}Ar$ analysis), empty circle (estimated/interpolated age based on the tephra depth within the drilling site and the assumption of a constant sedimentation rate) and triangle (orbitally tuned aged). Established correlations between tephra layers and dated eruptions at specific volcanoes in the CMER are reported within the last column on the right. Large proximal deposits observed along the eastern and western margin of the CMER and dated within this study (weighted mean ages are reported in Supplementary Tables 1 and 2) are reported in bold and capital letters.

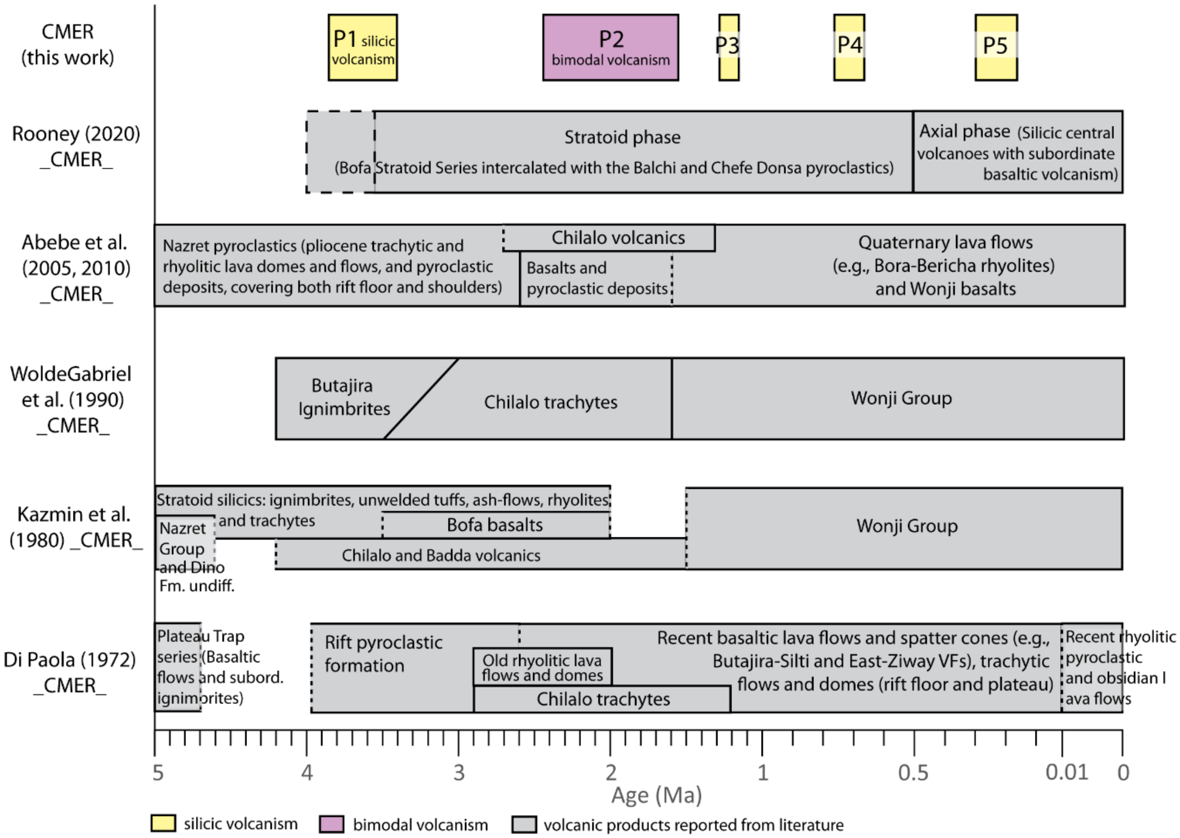

Supplementary Figure 7. Comparison between the reconstruction of the CMER volcanic activity obtained from this work and those inferred from previous studies in this sector of the rift. The chart is compiled from the geological maps of Di Paola et al.[46] and Kazmin et al.[47], and from the works of WoldeGabriel et al.[5], Abebe et al.[48,49] and Rooney[50]. We did not consider those works which do not have a comprehensive view of the central sector of the rift both on a temporal and areal point of view (i.e., works which focus on specific volcanic complexes, restricted areas or restricted periods of volcanic activity).

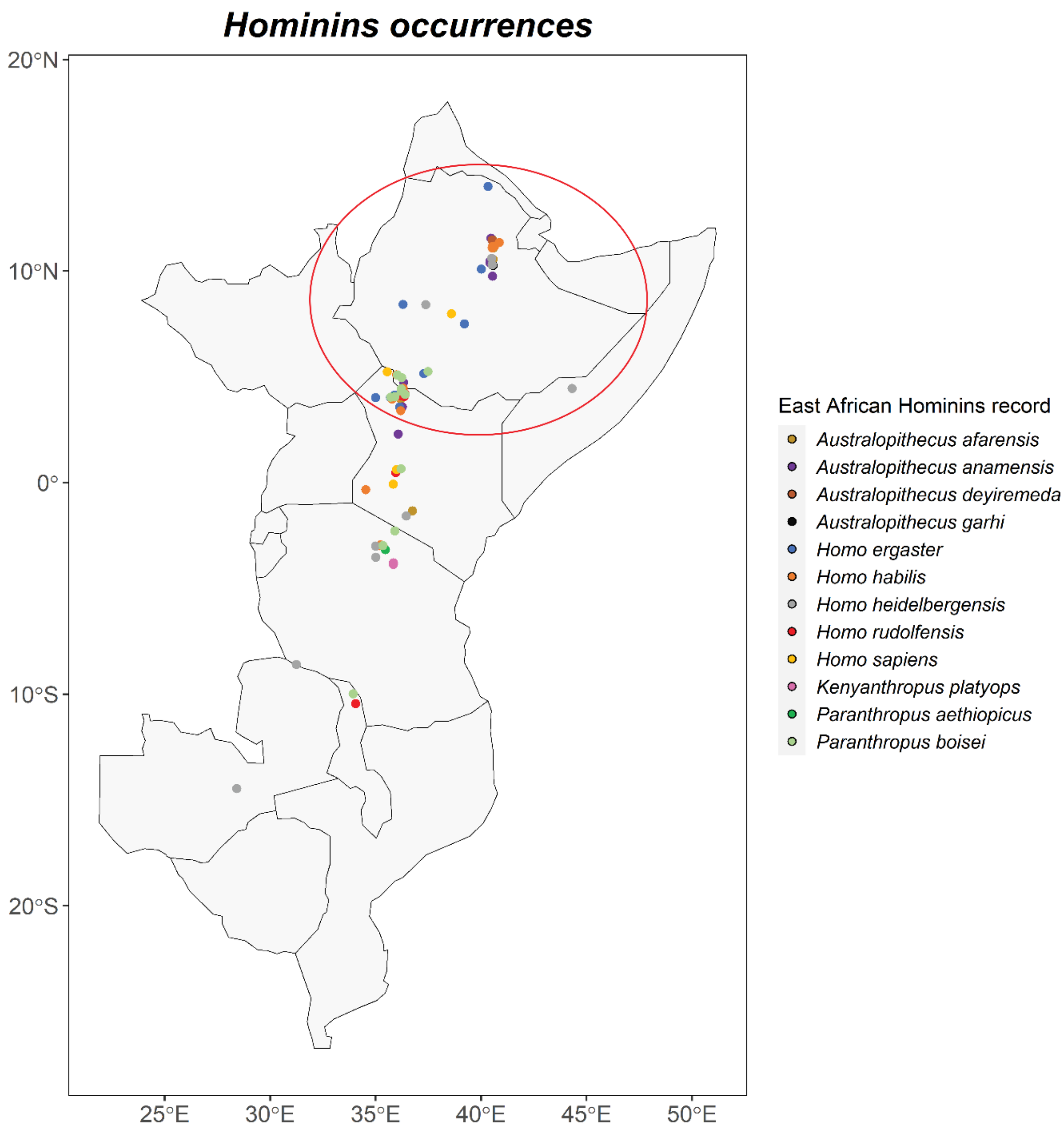

Supplementary Figure 8. Areal distribution of the hominins fossil record in East Africa considered to calculate the age intervals as reported in Fig. 4b of the main text. Age intervals were defined implementing the human dataset published by Timmermann et al.[51] with the fossil occurrences of hominins species cited in Supplementary Discussion 2 (ref. 51-73). The red ellipse identifies the hominins occurrences (coloured horizontal bars in Fig. 4b) within the restricted area (Ethiopia and proximal areas) potentially impacted by the volcanic activity studied in this work. The hominins occurrences located outside the red ellipse were used as a comparison tool with the fossil record in the whole East Africa (thin horizontal lines in Fig. 4b).

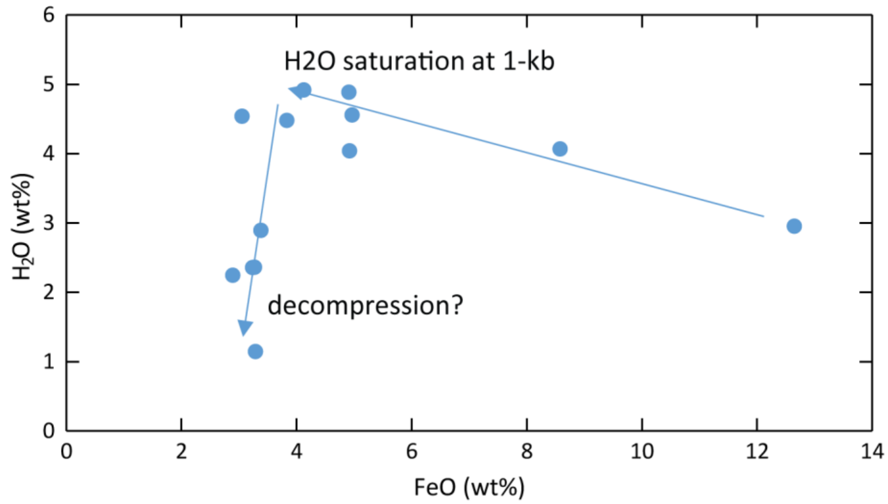

Supplementary Figure 9. Evolution of melt H_2O content with FeO content of melt inclusions.

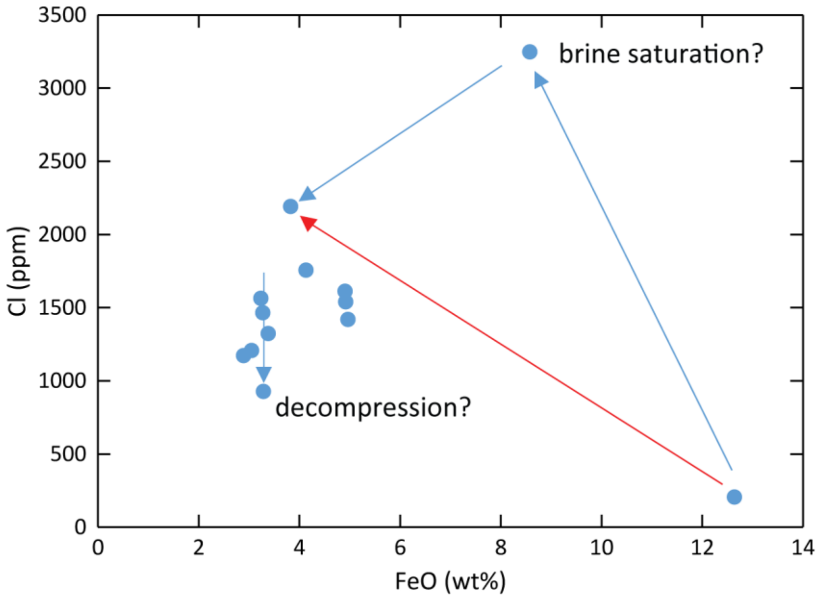

Supplementary Figure 10. Evolution of Cl content with FeO content of melt inclusions.

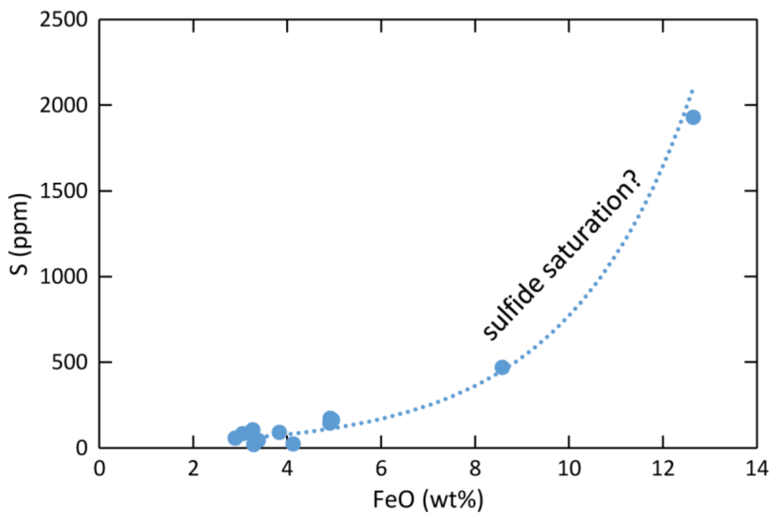

Supplementary Figure 11. Evolution of melt S content with FeO content of melt inclusions.

Supplementary Table 1. $^{40}Ar/^{39}Ar$ dataset with site location of the sample, unit name attribution, and lithology. Analysed phase: san (sanidine), plag (plagioclase), glass (glass fragments), gdm (groundmass fragments). The procedure of dating is indicated along with run number. Only a subset of the total number of runs performed for each sample has been considered in the determination of the WMA; this is specified as the number of steps included (n) over total measured (N). When multiple WMA are defined, the one marked with an asterisk represents the preferred age. Samples from the western margin are in italic.

Site	Unit name	Sample	Rock type	Phase	Dating procedure	Run number	WMA (Ma)			n/N	MSWD
H3	H3.A	ETZ01	welded ignimbrite	san	total fusion	N231.MS3	0.158	±	0.002	18/20	0.94
N7	N7.A	ETZ115	ignimbrite	san	total fusion	N350.MS3	0.162	±	0.003	11/21	1.36
A3	A3.A	ETZ149	unwelded ignimbrite	san	total fusion	N356.MS3	0.165	±	0.003	20/26	0.85
D8	D8.B	ETZ135	fallout	san	total fusion	N352.MS3	0.165	±	0.004	4/20	0.96
H5	H5.A	ETZ03	welded ignimbrite	san	total fusion	N232.MS3	0.165	±	0.002	17/19	1.46
C1	C1.B	ETZ20	welded ignimbrite	san	total fusion	N361.MS3+N238.MS3	0.169	±	0.003	20/20	0.45
A2	Kulumsa Ignimbrite	ETZ54	welded ignimbrite	san	total fusion	N261.MS3	0.182	±	0.003	17/17	0.58
A1	Kulumsa Ignimbrite	ETZ148bis	poorly welded facies of the ignimbrite	san	total fusion	N355.MS3	0.183	±	0.003	14/23	1.07
D3	D3.B	ETZ146	unwelded ash flow	san	total fusion	N354.MS3	0.283	±	0.003	21/22	1.16
D3	Katar Ignimbrite	ETZ12	welded ignimbrite	san	total fusion	N360.MS3+N259.MS3	0.287	±	0.002	14/20	1.66
E2	E2.A	ETZ27	welded ignimbrite	san	total fusion	N348.MS3	0.299	±	0.004	20/22	1.34
D3	D3.A	ETZ11	poorly welded ignimbrite	san	total fusion	N236.MS3	0.299	±	0.002	25/25	1.53
C3	C3.B	ETZ46	pumice bombs from ignimbrite	san	total fusion	N253.MS3	0.299	±	0.002	19/20	1.47
H1	H1.B	ETZ122	moderately welded ignimbrite	san	total fusion	N335.MS3	0.301	±	0.002	20/20	1.59
D2	Katar Ignimbrite	ETZ07	welded ignimbrite	san	total fusion	N233.MS3	0.303	±	0.003	14/15	1.57
A1	A1.C	ETZ57	vitrophyric facies of the ignimbrite	san	total fusion	N256.MS3	0.659	±	0.002	19/20	1.50
A1	A1.B	ETZ56	phaneritic fiamme from ignimbrite	san	total fusion	N255.MS3	0.677	±	0.002	15/20	1.64
C3	C3.A	ETZ45	pumice-rich ash flow	san	total fusion	N252.MS3	0.734	±	0.002	11/20	1.73
A1	A1.A	ETZ55B	black pumice bombs from ignimbrite	san	total fusion	N254.MS3	0.760	±	0.008	14/15	1.23
B7	Golja Ignimbrite	ETZ21	white pumice bombs from ignimbrite	san	total fusion	N358.MS3+N239-240	1.159	±	0.006	23/32	1.45
C4	Golja Ignimbrite	ETZ41B	dark pumice bombs from ignimbrite	san	total fusion	N364.MS3+N251.MS3	*1.195	±	0.008	7/20	1.78
							1.26	±	0.009	12/20	1.72
K5	*K2.A*	*ETZ79*	*fallout*	*san*	*total fusion*	*N329.MS3*	*1.196*	±	*0.004*	*9/18*	*1.87*
K6	*K6.A*	*ETZ80*	*moderately welded ignimbrite*	*san*	*total fusion*	*N330.MS3+N336.MS3*	*1.203*	±	*0.003*	*20/26*	*1.57*
C1	Kencherra Ignimbrite	ETZ17	unwelded basal facies	san	total fusion	N363.MS3+N260.MS3	*1.203	±	0.005	5/25	2.26
							1.243	±	0.004	6/25	2.01
H6	H6.A	ETZ125	poorly welded ignimbrite	san	total fusion	N351.MS3	1.224	±	0.004	15/23	1.49
I6	*I6.A*	*ETZ85*	*poorly welded ignimbrite*	*san*	total fusion	*N338.MS3*	*1.226*	±	*0.006*	*14/29*	*1.45*
D1	D1.A	ETZ145	welded ignimbrite	san	total fusion	N353.MS3	1.250	±	0.007	18/20	1.61
E3	Kencherra Ignimbrite	ETZ39	poorly foliated facies	san	total fusion	N249.MS3	1.263	±	0.004	15/17	1.67
D3	Kencherra Ignimbrite	ETZ09	foliated facies	san	total fusion	N234.MS3	1.270	±	0.004	15/17	1.79
E3	Kencherra Ignimbrite	ETZ40	vitrophyric facies	san	total fusion	N250.MS3	1.270	±	0.004	15/20	0.78
N4	N4.A	ETZ114	pumice bombs from pumice flow	san	total fusion	N349.MS3	1.293	±	0.006	20/20	1.31
B7	Chebi ash flow	ETZ22	ash flow	san	total fusion	N362.MS3+N241.MS3	1.545	±	0.004	13/23	1.61
C1	Chebi ash flow	ETZ14	pumice bombs from ash flow	san	total fusion	N237.MS3	1.592	±	0.003	19/20	1.36
B8	B8.D	ETZ153	ash flow	san	total fusion	N359.MS3	1.727	±	0.005	17/22	1.54
B8	B8.C	ETZ152	fallout	san	total fusion	N357.MS3	1.833	±	0.011	13/25	0.85
B3	B3.A	ETZ24	scoria	gdm	step heating	N264.MS3	*1.919	±	0.016	14/14	3.12
						N265.MS3	1.934	±	0.012	8/13	0.96
C1	C1.A	ETZ13	phaneritic basalt flow	plag	total fusion	N235.MS3	1.97	±	0.67	24/24	1.45
K1	*K1.A*	*ETZ82*	*fallout*	*san*	total fusion	*N337.MS3*	**2.071*	±	*0.005*	5/20	*0.86*
							2.124	±	*0.003*	13/20	*1.58*
K3	*K3.A*	*ETZ76*	*welded ignimbrite*	*san*	*total fusion*	*N328.MS3*	*2.222*	±	*0.004*	*13/20*	*1.67*
H2	H2.B	ETZ05	obsidian lava flow	glass	total fusion	N340.MS3	2.435	±	0.076	7/8	1.39
MK	*Melka Kunturé Ignimbrite*	*ETZ63*	*welded ignimbrite*	*san*	total fusion	*N323.MS3*	*3.152*	±	*0.006*	*13/20*	*1.77*
G3	MCT s.s.	ETZ89	welded facies	san	total fusion	N333.MS3	*3.412	±	0.004	15/39	1.57
							3.483	±	0.005	21/39	1.31
G3	MCT s.s.	ETZ90	unwelded top facies	san	total fusion	N334.MS3	*3.429	±	0.004	22/39	1.47
							3.502	±	0.005	16/39	1.32
E3	MCT s.s.	ETZ36	unwelded top facies	san	total fusion	N248.MS3	*3.452	±	0.008	5/27	2.02
							3.512	±	0.005	12/27	1.94
							3.562	±	0.005	10/27	1.58
G2	MCT s.s.	ETZ34	poorly welded to unwelded facies of the ignimbrite	san	total fusion	N243.MS3	*3.463	±	0.006	5/23	0.14
							3.539	±	0.005	12/23	1.52
G2	MCT s.s.	ETZ35	unwelded top facies	san	total fusion	N244.MS3	*3.511	±	0.005	15/27	1.97
							3.581	±	0.005	12/27	1.58
J3	*Kella- Butajira Ignimbrite*	*ETZ61*	*welded ignimbrite*	*san*	*total fusion*	*N257.MS3*	**3.537*	±	*0.004*	*20/32*	*1.53*
							3.586	±	*0.005*	*12/32*	*1.66*
G2	MCT s.s.	ETZ33	welded facies	san	total fusion	N242.MS3	3.552	±	0.005	21/25	1.18
I4	*Kella- Butajira Ignimbrite*	*ETZ62*	*welded ignimbrite*	*san*	*total fusion*	*N258.MS3*	*3.578*	±	*0.004*	*17/21*	*1.27*
K3	*Worabe ash flow*	*ETZ75*	*poorly welded ash flow*	*san*	*total fusion*	*N327.MS3*	*3.605*	±	*0.006*	*10/19*	*0.64*
H1	H1.A	ETZ123	poorly welded ignimbrite	san	total fusion	N339.MS3	3.691	±	0.007	12/19	0.90
J11	*Guraghe Ignimbrite*	*ETZ72*	*moderately welded ignimbrite*	*san*	*total fusion*	*N326.MS3*	*3.846*	±	*0.007*	*12/20*	*1.52*
J7	*Guraghe Ignimbrite*	*ETZ67*	*moderately welded ignimbrite*	*san*	*total fusion*	*N324.MS3*	*3.855*	±	*0.007*	*16/20*	*1.52*
J2	*J2.A*	*ETZ58*	*basalt flow*	*gdm*	*step heating*	*N266.MS3*	*9.650*	±	*0.030*	*8/19*	*3.76*
						N267.MS3	**9.410*	±	*0.080*	*11/18*	*0.97*
						N268.MS3	*9.440*	±	*0.040*	*16/17*	*6.57*
J6	*J6.B*	*ETZ69*	*tephra*	*san*	*total fusion*	*N325.MS3*	*10.224*	±	*0.035*	*9/20*	*1.33*

Supplementary Table 2. Mean and preferred age (in bold) between multiple samples of the same volcanic units. Volcanic units from the western margin are in italic.

Unit name	Sample	Rock type	WMA (Ma)					
			mean age			*preferred age		
Kulumsa Ign.	ETZ54-ETZ148	ignimbrite	0.183	±	0.003	**0.182**	**±**	**0.003**
Katar Ign.	ETZ07-ETZ12	ignimbrite	0.295	±	0.002	**0.287**	**±**	**0.002**
Golja Ign.	ETZ21-ETZ41B	pumice bombs from ign.	1.177	±	0.007	**1.159**	**±**	**0.006**
Kencherra Ign.	ETZ09, ETZ39-40	ignimbrite	1.268	±	0.004	**1.263**	**±**	**0.004**
Chebi ash flow	ETZ14-ETZ22	pumices from ash flow	1.569	±	0.004	**1.545**	**±**	**0.004**
B3.A unit	ETZ24	scoria	1.927	±	0.014	**1.919**	**±**	**0.016**
MCT s.s.	ETZ33-36, ETZ89-90	ignimbrite	3.470	±	0.005	**3.412**	**±**	**0.004**
Kella- Butajira Ign.	*ETZ61-ETZ62*	*ignimbrite*	*3.557*	±	*0.004*	***3.537***	**±**	***0.004***
Guraghe Ign.	*ETZ67-ETZ72*	*ignimbrite*	*3.851*	±	*0.007*	***3.846***	**±**	***0.007***
J2.A unit	*ETZ58B*	*basalt flow*	*9.500*	±	*0.054*	***9.410***	**±**	***0.080***

Supplementary Table 3. Average element concentrations and standard deviations of the analysed melt inclusions. “n” indicates the number of melt inclusion considered. Zr concentration was determined by LA-ICP-MS using an excimer RESOlution ArF 193 nm laser ablation system (Resonetics) coupled to an Agilent 8900 Triple Quadrupole ICP-MS, available at the ISTO-CNRS facility. H_2O refers to the estimated water content. Abbreviations used in the type and description: MI= melt inclusion; gm= groundmass (in bold); g.= glassy; g.v.= glassy vesicular; p.r.= partially recrystallized; s.r.= spherultic recrystallization; Qz: quartz; San: sanidine; Plag: plagioclase. The melt inclusions trapped in plagioclase crystals are basaltic; the rest of the melt inclusions and the groundmass glass is rhyolitic in composition.

				Zr (ppm)		SiO_2 (wt.%)		Cl (wt.%)		F (wt.%)		SO_3 (wt.%)		H_2O (wt.%)	
Sample	Type	Description	n	mean	st. dev.	mean	st. dev.	mean	st. dev.	mean	st. dev.	mean	st. dev.	mean	st. dev.
ETZ31	MI	g.v. MI	11	1001.876	23.245	76.256	0.248	0.147	0.009	0.054	0.013	0.027	0.012	2.362	1.103
ETZ31	MI	p.r. MI	10	977.506	20.699	76.450	0.304	0.121	0.018	0.067	0.011	0.021	0.013	4.542	0.588
ETZ31	**gm**	**glass border**	**2**	**955.670**	**33.531**	**76.602**	**0.361**	**0.156**	**0.004**	**0.035**	**0.036**	**0.022**	**0.006**	**2.359**	**0.840**
ETZ90	MI	g. MI	7	1569.697	135.717	75.940	0.601	0.132	0.033	0.002	-	0.011	0.006	2.893	1.316
ETZ90	MI	g.v. MI	4	1117.495	46.902	76.184	0.096	0.117	0.018	0.013	-	0.015	0.008	2.246	0.562
ETZ90	**gm**	**glass border**	**1**	**1515.750**	**-**	**75.295**	**-**	**0.176**	**-**	**-**	**-**	**0.006**	**-**	**4.917**	**-**
ETZ30	MI	g. MI with s.r.	14	-	-	75.730	0.197	0.219	0.032	-	-	0.023	0.014	4.479	0.382
ETZ136	MI	g. MI (in Qz)	7	1018.423	212.612	75.183	0.694	0.161	0.038	0.017	0.010	0.036	0.015	4.888	1.835
ETZ136	MI	g. MI (in Qz)	1	1681.650	-	71.419	-	0.325	-	0.042	-	0.118	-	4.068	-
ETZ136	MI	g. MI (in Qz)	1	-	-	69.318	-	0.093	-	0.182	-	0.005	-	1.146	-
ETZ136	MI	g. MI (in San)	3	959.780	-	74.685	0.336	0.142	0.022	-	-	0.041	0.019	4.560	0.782
ETZ136	**gm**	**glass border**	**1**	**861.580**	**-**	**74.909**	**-**	**0.154**	**-**	**-**	**-**	**0.043**	**-**	**4.042**	**-**
ETZ136	MI	g. MI (in Plag)	5	94.290	14.347	47.591	0.533	0.021	0.014	-	-	0.483	0.081	2.956	0.244

Supplementary Data 1 (separate file)

Review of existing ages on distal tephra and correlation.

Supplementary Data 2 (separate file)

Melt inclusions geochemistry. The table indicates the sample, the type of material analysed (melt inclusion - MI or groundmass - gm) and the hosting crystal and reports the major element and volatile concentrations of each melt inclusion.

Supplementary Data 3 (separate file)

Samples overview reporting the sample name, site location, belonging unit name and brief description of the depositional facies.

Supplementary Data 4 (separate file)

Primary total-gas Ar/Ar ratio data including the irradiation parameters (J) and all isotopes from 36Ar to 40Ar. FOM = figure of merit.

Supplementary References

1. L. Telesca, V. Cuomo, V. Lapenna, & M. Macchiato, On the methods to identify clustering properties in sequences of seismic time-occurrences. *Journal of seismology*, 6(1), 125-134 (2002).
2. L. Telesca, Time-clustering of natural hazards. *Natural hazards*, 40, 593-601 (2007).
3. W. Marzocchi, & L. Zaccarelli, A quantitative model for the time-size distribution of eruptions. *Journal of Geophysical Research: Solid Earth*, 111(B4) (2006).
4. W. Hutchison, R. Fusillo, D. M. Pyle, T. A. Mather, J. D. Blundy, J. Biggs, ... & A. T. Calvert, A pulse of mid-Pleistocene rift volcanism in Ethiopia at the dawn of modern humans. *Nature Communications*, 7(1), 1-12 (2016a).
5. G. WoldeGabriel, J. L. Aronson, & R. C. Walter, Geology, geochronology, and rift basin development in the central sector of the Main Ethiopia Rift. *Geological Society of America Bulletin*, 102(4), 439-458 (1990).
6. S. L. Quane, & J. K. Russell, Ranking welding intensity in pyroclastic deposits. *Bulletin of Volcanology*, 67(2), 129-143 (2005).
7. C. E. Lesher, & F. J. Spera, Thermodynamic and transport properties of silicate melts and magma. In *The encyclopedia of volcanoes* (pp. 113-141). Academic Press, (2015).
8. F. Iddon, & M. Edmonds, Volatile-rich magmas distributed through the upper crust in the Main Ethiopian Rift. *Geochemistry*, *Geophysics*, *Geosystems*, 21(6), e2019GC008904 (2020).
9. D. S. Stamps, C. Kreemer, R. Fernandes, T. A. Rajaonarison, & G. Rambolamanana, Redefining east African rift system kinematics. *Geology*, 49(2), 150-155 (2021).
10. Z. Franceschini, Large explosive volcanic events and tectonic evolution of continental rift in the Main Ethiopian Rift, East Africa. *PhD thesis*, (2022).
11. N. Vogel, S. Nomade, A. Negash, & P. R. Renne, Forensic 40Ar/39Ar dating: a provenance study of Middle Stone Age obsidian artifacts from Ethiopia. *Journal of Archaeological Science*, 33(12), 1749-1765 (2006).
12. R. S. J. Sparks, & G. P. L. Walker, The significance of vitric-enriched air-fall ashes as- sociated with crystal-enriched ignimbrites. *Journal of Volcanology and Geothermal Research*, 2, 329–341 (1977).
13. R. S. J. Sparks, P. W. Francis, R. D. Hamer, R. J. Pankhurst, L. O. O'Callaghan, R. S. Thorpe, R. Page, Ignimbrites of the Cerro Galan Caldera, NW Argentina. *Journal of Volcanology and Geothermal Research*, 24, 205–248 (1985).

14. R. Cas, & J. Wright, Volcanic successions: Modern and ancient. A geological approach to processes, products and successions. *Springer Science & Business Media* (2012).

15. W. I. Rose, & C. A. Chesner, Dispersal of ash in the great Toba eruption, 75 ka. *Geology*, 15, 913–917 (1987).

16. A. W. Woods, & K. Wohletz, Dimensions and dynamics of co-ignimbrite eruption columns. *Nature*, 350(6315), 225-227 (1991).

17. A. J. W. Gleadow, Fission track age of the KBS Tuff and associated hominid remains in northern Kenya. *Nature*, 284(5753), 225-230 (1980).

18. I. McDougall, K-Ar and 4~Ar/39Ar dating of the hominid-bearing Pliocene-Pleistocene sequence at Koobi Fora, Lake Turkana, Northern Kenya. *Geological Society of America Bulletin*, 96, 159-175 (1985).

19. B. Haileab, & F. H. Brown, Turkana Basin-Middle Awash Valley correlations and the age of the Sagantole and Hadar formations. *Journal of Human Evolution*, 22(6), 453-468 (1992).

20. F. H. Brown, A. M. Sarna-Wojcicki, C. E. Meyer, & B. Haileab, Correlation of Pliocene and Pleistocene tephra layers between the Turkana Basin of East Africa and the Gulf of Aden. *Quaternary International*, 13, 55-67 (1992).

21. I. McDougall, & F. H. Brown, Precise 40Ar/39Ar geochronology for the upper Koobi Fora Formation, Turkana basin, northern Kenya. *Journal of the Geological Society*, 163(1), 205-220 (2006).

22. I. McDougall, & F. H. Brown, Geochronology of the pre-KBS tuff sequence, Omo Group, Turkana Basin. *Journal of the Geological Society*, 165(2), 549-562 (2008).

23. F. H. Brown, & I. Mcdougall, Geochronology of the Turkana depression of northern Kenya and southern Ethiopia. *Evolutionary Anthropology: Issues, News, and Reviews*, 20(6), 217-227 (2011).

24. I. McDougall, F. H. Brown, P. M. Vasconcelos, B. E. Cohen, D. S. Thiede, & M. J. Buchanan, New single crystal 40Ar/39Ar ages improve time scale for deposition of the Omo Group, Omo–Turkana Basin, East Africa. *Journal of the Geological Society*, 169(2), 213-226 (2012).

25. Y. Beyene, S. Katoh, G. WoldeGabriel, W. K. Hart, K. Uto, M. Sudo, ... & B. Asfaw, The characteristics and chronology of the earliest Acheulean at Konso, Ethiopia. *Proceedings of the National Academy of Sciences*, 110(5), 1584-1591 (2013).

26. G. WoldeGabriel, W. K. Hart, S. Katoh, Y. Beyene, & G. Suwa, Correlation of Plio–Pleistocene tephra in Ethiopian and Kenyan rift basins: Temporal calibration of geological features and hominid fossil records. *Journal of Volcanology and Geothermal Research*, 147(1-2), 81-108 (2005).

27. G. WoldeGabriel, T. Endale, T. D. White, N. Thouveny, W. K. Hart, P. R. Renne, & B. Asfaw, The role of tephra studies in African paleoanthropology as exemplified by the Sidi Hakoma Tuff. *Journal of African Earth Sciences*, 77, 41-58 (2013).

28. D. Phillips, E. Matchan, A. Gleadow, F. Brown, I. McDougall, T. Cerling, ... & L. Leakey, 40Ar/39Ar eruption ages of Turkana Basin tuffs: millennial scale resolution constrains paleoclimate proxy tuning models and hominin fossil ages. *Journal of the Geological Society*, 180(4), jgs2022-171 (2023).

29. I. McDougall, F. H. Brown, & J. G. Fleagle, Stratigraphic placement and age of modern humans from Kibish, Ethiopia. *Nature*, 433(7027), 733-736 (2005).

30. C. M. Vidal, C. S. Lane, A. Asrat, D. N. Barfod, D. F. Mark, E. L. Tomlinson, … & C. Oppenheimer, Age of the oldest known Homo sapiens from eastern Africa. *Nature*, 601, 579–583 (2022a).

31. S. Katoh, S. Nagaoka, G. WoldeGabriel, P. Renne, M. G. Snow, Y. Beyene, & G. Suwa, Chronostratigraphy and correlation of the Plio-Pleistocene tephra layers of the Konso Formation, southern Main Ethiopian Rift, Ethiopia. *Quaternary Science Reviews*, 19(13), 1305-1317 (2000).

32. J. D. Clark, Y. Beyene, G. WoldeGabriel, W. K. Hart, P. R. Renne, H. Gilbert, ... & T. D. White, T. D. Stratigraphic, chronological and behavioural contexts of Pleistocene Homo sapiens from Middle Awash, Ethiopia. *Nature*, 423(6941), 747-752 (2003).

33. F. H. Brown, B. Haileab, & I. McDougall, Sequence of tuffs between the KBS Tuff and the Chari Tuff in the Turkana Basin, Kenya and Ethiopia. *Journal of the Geological Society*, 163(1), 185-204 (2006).

34. L. E. Morgan, & P. R. Renne, Diachronous dawn of Africa's Middle Stone Age: new 40Ar/39Ar ages from the Ethiopian Rift. *Geology*, 36(12), 967-970 (2008).

35. C. M. Vidal, K. Fontijn, C.S. Lane, A. Asrat, D. Barfod, E. L. Tomlinson, … & C. Oppenheimer, Geochronology and glass geochemistry of major pleistocene eruptions in the Main Ethiopian Rift: Towards a regional tephrostratigraphy. *Quaternary Science Reviews*, 290:107601 (2022b).

36. M. Taieb, D. C. Johanson, Y. Coppens, & J. L. Aronson, Geological and palaeontological background of Hadar hominid site, Afar, Ethiopia. *Nature*, 260(5549), 289-293 (1976).

37. R. C. Walter, Age of Lucy and the First Family: single-crystal 40Ar/39Ar dating of the Denen Dora and lower Kada Hadar members of the Hadar Formation, Ethiopia. *Geology*, 22(1), 6-10 (1994).

38. D. C. Roman, C. Campisano, J. Quade, E. DiMaggio, J. R. Arrowsmith, & C. Feibel, Composite tephrostratigraphy of the Dikika, Gona, Hadar, and Ledi-Geraru project

areas, northern Awash, Ethiopia. *The geology of early humans in the horn of Africa, Special Paper*, 446, 119-134 (2008).

39. A. L. Deino, G. R. Scott, B. Saylor, M. Alene, J. D. Angelini, & Y. Haile-Selassie, 40Ar/39Ar dating, paleomagnetism, and tephrochemistry of Pliocene strata of the hominid-bearing Woranso-Mille area, west-central Afar Rift, Ethiopia. *Journal of Human Evolution*, 58(2), 111-126 (2010).

40. A. M. Sarna-Wojcicki, C. E. Meyer, P. H. Roth, & F. H. Brown, Ages of tuff beds at East African early hominid sites and sediments in the Gulf of Aden. *Nature*, 313(6000), 306-308 (1985).

41. P. B. deMenocal, & F. H. Brown, Pliocene tephra correlations between East African hominid localities, the Gulf of Aden, and the Arabian Sea. *Hominid evolution and climatic change in Europe*, 1, 23-54 (1999).

42. S. J. Feakins, F. H. Brown, & P. B. demenocal, Plio-Pleistocene microtephra in DSDP site 231, Gulf of Aden. *Journal of African Earth Sciences*, 48(5), 341-352 (2007).

43. R. C. Walter, & J. L. Aronson, Age and source of the Sidi Hakoma tuff, Hadar formation, Ethiopia. *Journal of Human Evolution*, 25, 229-240 (1993).

44. T. D. White, W. K. Hart, R. C. Walter, G. WoldeGabriel, J. de Heinzelin, J. D. Clark, ... & E. Vrba, New discoveries of Australopithecus at Maka in Ethiopia. *Nature*, 366(6452), 261-265 (1993).

45. A. Z. Tadesse, K. Fontijn, A. A. Melaku, E. F. Gebru, V. C. Smith, E. Tomlinson, D. Barfod, P. Gopon, F. Bégué, L. Caricchi, P. Laha, H. Terryn, S. Gudbrandsson, G. Yirgu, & D. Ayalew, Eruption frequency and magnitude in a geothermally active continental rift: The Bora-Baricha-Tullu Moye volcanic complex, Main Ethiopian Rift. *Journal of Volcanology and Geothermal Research*, 423, 107471 (2022).

46. G. M. Di Paola, The Ethiopian Rift Valley (between 7 00′ and 8 40′ lat. north). Bulletin Volcanologique, 36(4), 517-560 (1972).

47. V. Kazmin, Geodynamic control of rift volcanism. *Geologische Rundschau*, 69(3), 757-769 (1980).

48. T. Abebe, P. Manetti, M. Bonini, G. Corti, F. Innocenti, F. Mazzarini, Z. Pecksay, Geological map (scale 1:200,000) of the Northern Main Ethiopian Rift and its implications for the volcano-tectonic evolution of the rift. *Geol. Soc. Am* (2005).

49. T. Abebe, M. L. Balestrieri, & G. Bigazzi, The central Main Ethiopian rift is younger than 8 Ma: Confirmation through apatite fission-track thermochronology. *Terra Nova*, 22(6), 470-476 (2010).

50. T. O. Rooney, The Cenozoic magmatism of East Africa: Part II–Rifting of the mobile belt. *Lithos*, 360, 105291 (2020).

51. A. Timmermann, K. S. Yun, P. Raia, J. Ruan, A. Mondanaro, E. Zeller, ... & A. Ganopolski, Climate effects on archaic human habitats and species successions. *Nature*, 604(7906), 495-501 (2022).

52. A. Du, J. Rowan, S. C. Wang, B. A. Wood, & Z. Alemseged, Statistical estimates of hominin origination and extinction dates: A case study examining the Australopithecus anamensis–afarensis lineage. *Journal of human evolution*, 138, 102688 (2020).

53. M. G. Leakey, C. S. Feibel, I. McDougall, C. Ward, & A. Walker, New specimens and confirmation of an early age for Australopithecus anamensis. *Nature*, 393(6680), 62-66 (1998).

54. C. J. Campisano, & C. S. Feibel, Connecting local environmental sequences to global climate patterns: evidence from the hominin-bearing Hadar Formation, Ethiopia. *Journal of Human Evolution*, 53(5), 515-527 (2007).

55. Y. Haile-Selassie, L. Gibert, S. M. Melillo, T. M. Ryan, M. Alene, A. Deino, ... & B. Z. Saylor, New species from Ethiopia further expands Middle Pliocene hominin diversity. *Nature*, 521(7553), 483-488 (2015).

56. M. G. Leakey, F. Spoor, F. H. Brown, P. N. Gathogo, C. Kiarie, L. N. Leakey, & I. McDougall, New hominin genus from eastern Africa shows diverse middle Pliocene lineages. *In Human Evolution Source Book* (pp. 118-127). Routledge (2016).

57. A. L. Deino, 40 Ar/39 Ar dating of Laetoli, Tanzania. *Paleontology and geology of Laetoli: human evolution in context: volume 1: geology, geochronology, paleoecology and paleoenvironment*, 77-97 (2011).

58. C. S. Feibel, F. H. Brown, & I. McDougall, Stratigraphic context of fossil hominids from the Omo group deposits: Northern Turkana Basin, Kenya and Ethiopia. *American Journal of Physical Anthropology*, 78(4), 595-622 (1989).

59. J. G. Wynn, Z. Alemseged, R. Bobe, F. E. Grine, E. W. Negash, & M. Sponheimer, Isotopic evidence for the timing of the dietary shift toward C4 foods in eastern African Paranthropus. *Proceedings of the National Academy of Sciences*, 117(36), 21978-21984 (2020).

60. M. Dominguez-Rodrigo, T. R. Pickering, E. Baquedano, A. Mabulla, D. F. Mark, C. Musiba, ... & A. Pérez-González, First partial skeleton of a 1.34-million-year-old Paranthropus boisei from Bed II, Olduvai Gorge, Tanzania. *PLoS One*, 8(12) (2013).

61. B. Asfaw, T. White, O. Lovejoy, B. Latimer, S. Simpson, & G. Suwa, Australopithecus garhi: a new species of early hominid from Ethiopia. *Science*, 284(5414), 629-635 (1999).

62. D. S. Strait, & F. E. Grine, The systematics of Australopithecus garhi. *Ludus Vitalis*, 9(15), 109-135 (2001).

63. B. Villmoare, W. H. Kimbel, C. Seyoum, C. J. Campisano, E. N. DiMaggio, J. Rowan, ... & K. E. Reed, Early Homo at 2.8 Ma from Ledi-Geraru, Afar, Ethiopia. *Science*, 347(6228), 1352-1355 (2015).

64. Neves, W., Senger, M. H., Rocha, G., Suesdek, L., & Hubbe, M. (2023). Ledi-Geraru strikes again: Morphological affinities of the LD 350-1 mandible with early Homo. *Anais da Academia Brasileira de Ciências*, 95, e20230032.

65. I. de la Torre, A. Benito-Calvo, C. Martín-Ramos, L. J. McHenry, R. Mora, J. K. Njau, ... & H. Stollhofen, New excavations in the MNK Skull site, and the last appearance of the Oldowan and Homo habilis at Olduvai Gorge, Tanzania. *Journal of Anthropological Archaeology*, 61, 101255 (2021).

66. D. Argue, Homo rudolfensis. *Encyclopedia of Evolutionary Psychological Science* (2017).

67. M. G. Leakey, F. Spoor, M. C. Dean, C. S. Feibel, S. C. Antón, C. Kiarie, & L. N. Leakey, New fossils from Koobi Fora in northern Kenya confirm taxonomic diversity in early Homo. *Nature*, 488(7410), 201-204 (2012).

68. A. L. Deino, & A. Hill, 40Ar/39Ar dating of Chemeron Formation strata encompassing the site of hominid KNM-BC 1, Tugen Hills, Kenya. *Journal of Human Evolution*, 42(1-2), 141-151 (2002).

69. F. Schrenk, T. G. Bromage, C. G. Betzler, U. Ring, & Y. M. Juwayeyi, Oldest Homo and Pliocene biogeography of the Malawi rift. *Nature*, 365(6449), 833-836 (1993).

70. A. I. Herries, J. M. Martin, A. B. Leece, J. W. Adams, G. Boschian, R. Joannes-Boyau, ... & C. Menter, Contemporaneity of australopithecus, paranthropus, and early homo erectus in South Africa. *Science*, 368(6486), eaaw7293 (2020).

71. C. J. Lepre, & D. V. Kent, Chronostratigraphy of KNM-ER 3733 and other Area 104 hominins from Koobi Fora. *Journal of human evolution*, 86, 99-111 (2015).

72. A. Profico, F. Di Vincenzo, G. Lorenza, P. Marcello, & G. Manzi, Filling the gap. Human cranial remains from Gombore II (Melka Kunture, Ethiopia; ca. 850 ka) and the origin of Homo heidelbergensis. *Journal of Anthropological Sciences*, 94, 41-63 (2016).

73. P. Raia, A. Mondanaro, M. Melchionna, M. Di Febbraro, J. A. Diniz-Filho, T. F. Rangel, ... & L. Rook, Past extinctions of Homo species coincided with increased vulnerability to climatic change. *One Earth*, 3(4), 480-490 (2020).

74. Irvine, T. N., & Baragar, W. R. A. (1971). A guide to the chemical classification of the common volcanic rocks. Canadian journal of earth sciences, 8(5), 523-548.

75. F. Iddon, & M. Edmonds, Volatile-rich magmas distributed through the upper crust in the Main Ethiopian Rift. *Geochemistry, Geophysics, Geosystems*, 21(6), e2019GC008904 (2020).

76. B. Scaillet, & R. Macdonald, Phase relations of peralkaline silicic magmas and petrogenetic implications. *Journal of Petrology*, 42(4), 825-845 (2001).

77. P. Romano, J. C. White, A. Ciulla, I. Di Carlo, C. D'Oriano, P. Landi, P., & S. G. Rotolo, Volatiles and trace elements content in melt inclusions from the zoned Green Tuff ignimbrite (Pantelleria, Sicily): petrological inferences. *Ann. Geophys.*, 62(1) (2019).

78. P. Romano, I. Di Carlo, J. Andújar, & S. G. Rotolo, Water solubility in trachytic and pantelleritic melts: an experimental study. *Comptes Rendus. Géoscience*, 353(S2), 1-17 (2021).

79. K. Iacovino, K. Ju-Song, T. Sisson, J. Lowenstern, R. Kuk-Hun, J. Jong-Nam, ... & R. Kum-Ran, Quantifying gas emissions from the "Millennium eruption" of Paektu volcano, democratic People's Republic of Korea/China. *Science advances*, 2(11), e1600913 (2016).

80. Di Carlo, S. G. Rotolo, B. Scaillet, V. Buccheri, & M. Pichavant, Phase equilibrium constraints on pre-eruptive conditions of recent felsic explosive volcanism at Pantelleria Island, Italy. *Journal of Petrology*, 51(11), 2245-2276 (2010).

81. B. Scaillet, F. Holtz, & M. Pichavant, Experimental constraints on the formation of silicic magmas. *Elements*, 12(2), 109-114 (2016).

82. J. E. Thines, I. A. Ukstins, C. Wall, & M. Schmitz, Volumetric extrusive rates of silicic supereruptions from the Afro-Arabian large igneous province. *Nature communications*, 12(1), 1-9 (2021).

83. B. Scaillet, B. Clemente, B. W. Evans, & M. Pichavant, Redox control of sulfur degassing in silicic magmas. *Journal of Geophysical Research: Solid Earth*, 103(B10), 23937-23949 (1998).

84. P.J. Wallace, Volcanic SO2 emissions and the abundance and distribution of exsolved gas in magma bodies. *Journal of Volcanology and Geothermal Research*, 108(1-4), 85-106 (2001).

85. J. C. White, D. F. Parker, & M. Ren, The origin of trachyte and pantellerite from Pantelleria, Italy: insights from major element, trace element, and thermodynamic modelling. *Journal of Volcanology and Geothermal Research*, 179(1-2), 33-55 (2009).

86. T. Thordarson, S. Self, N. Oskarsson, & T. Hulsebosch, Sulfur, chlorine, and fluorine degassing and atmospheric loading by the 1783–1784 AD Laki (Skaftár Fires) eruption in Iceland. *Bulletin of Volcanology*, 58, 205-225 (1996).

87. J. Hansen, A. Lacis, R. Ruedy, & M. Sato, Potential climate impact of Mount Pinatubo eruption. *Geophysical Research Letters*, 19(2), 215-218 (1992).

88. P. Minnis, E. F. Harrison, L. L. Stowe, G. G. Gibson, F. M. Denn, D. R. Doelling, & W. L. Smith Jr, Radiative climate forcing by the Mount Pinatubo eruption. *Science*, 259(5100), 1411-1415 (1993).

89. C. Oppenheimer, Limited global change due to the largest known Quaternary eruption, Toba≈ 74 kyr BP?. *Quaternary Science Reviews*, 21(14-15), 1593-1609 (2002).

90. B. Harris, The potential impact of super-volcanic eruptions on the Earth's atmosphere. *Weather*, 63(8), 221-225 (2008).

91. D. W. Thompson, & S. Solomon, Understanding recent stratospheric climate change. *Journal of Climate*, 22(8), 1934-1943 (2009).

92. C. Timmreck, Modeling the climatic effects of large explosive volcanic eruptions. *Wiley Interdisciplinary Reviews: Climate Change*, 3(6), 545-564 (2012).